



# Moment Tensor-Based Approach for Acoustic Emission Simulation in Brittle Rocks Using Combined Finite-Discrete Element Method (FDEM)

Weibing Cai<sup>1</sup> · Ke Gao<sup>1,2</sup> · Shan Wu<sup>1</sup> · Wei Long<sup>3,4</sup>

Received: 13 July 2022 / Accepted: 5 February 2023

© The Author(s), under exclusive licence to Springer-Verlag GmbH Austria, part of Springer Nature 2023

## Abstract

Acoustic emission (AE), a phenomenon of elastic waves released by localized fracture generation, has been extensively utilized as an effective tool for monitoring rock failure processes in many rock mechanics related fields. Within the framework of the combined finite-discrete element method (FDEM), we develop a new AE simulation technique based on moment tensor theory considering the clustering effect of microcracks. The technique first integrates forces around the AE source to obtain the moment tensor, and then estimates the AE magnitude associated with the acquired moment tensor. In addition to quantifying the seismic source mechanisms of the modeled AE events, the technique can also distinguish fracture types based on moment tensor decomposition approaches when an AE event contains multiple microcracks. The effectiveness of the newly developed approach for capturing the distribution of AE event magnitude is firstly verified by establishing a heterogeneous rock model under uniaxial compressive load. Then, we perform four typical tests to validate the effectiveness of the proposed approach for distinguishing the source mechanism of microcracks, and further revise the traditional criterion to better accommodate the discrimination of the full spectrum of AE source types. Furthermore, the fractures generated in the heterogeneous model demonstrate the capability of the moment tensor decomposition approach in distinguishing macrofracture types on laboratory scales. As an exemplar application, we also establish a numerical model to analyze the failure mechanism in a bridge region of two pre-existing flaws in a rock specimen through laboratory-scale uniaxial compression tests. The work may provide a new means to analyze fracturing and failure in rocks and the associated seismic behaviors.

## Highlights

- Moment tensor-based AE simulation approach is realized in FDEM for the first time.
- A clustering algorithm to integrate spatially and temporally connected microcracks is implemented.
- The effectiveness of the proposed approach for capturing AE event magnitude is verified.
- The proposed approach's capability to distinguish macroscopic fracture types is validated.
- The traditional criterion is modified to better discriminate full-spectrum AE source types.

---

✉ Ke Gao  
gaok@sustech.edu.cn

<sup>1</sup> Department of Earth and Space Sciences, Southern University of Science and Technology, Shenzhen 518055, Guangdong, China

<sup>2</sup> Guangdong Provincial Key Laboratory of Geophysical High-Resolution Imaging Technology, Southern University of Science and Technology, Shenzhen 518055, Guangdong, China

<sup>3</sup> Research Institute of Tsinghua University in Shenzhen, Shenzhen 518057, Guangdong, China

<sup>4</sup> iCore Group Inc., Shenzhen 518057, Guangdong, China

**Keywords** Combined finite-discrete element method (FDEM) · Acoustic emission · Numerical simulation · Moment tensor · Rock fracture

## 1 Introduction

Acoustic emission (AE, or microseismicity on field scale) is a phenomenon of transient elastic wave radiation in brittle rocks when subjected to external loadings (Lockner 1993). The generation of AE is often accompanied by the rapid release of localized strain energy associated with irreversible local deformations or damages, such as cracks initiation and grain boundary slips. In the excavation of many rock engineering projects (e.g., tunnel, rock slope, and unconventional energy exploitation), AE has been widely used to monitor the characteristics of fracturing processes and failure patterns in rock masses, and can also provide early warnings for safe engineering constructions. Additionally, AE poses self-similar and scale-invariant statistics from the laboratory scale of rock fracturing to the crustal scale of tectonic earthquakes (Hanks 1992). Therefore, investigating the spatial–temporal evolution and source mechanisms of AE events is crucial for predicting the failure mechanism of rock masses and even providing insights into the characteristics associated with seismic activities.

In laboratory studies, AE has been widely employed as an effective tool for evaluating rock failure and pinpointing fracture locations (Guo and Wong 2021; Tang et al. 2020; Wang et al. 2021b), which offers advantages of investigating damage processes without perturbing rock masses (Cai et al. 2007). The staged character of brittle fracturing is commonly obtained based on AE distributions with time, and the spatial evolution of AE can be analyzed by introducing the fractal theory to describe certain irregular phenomena and characterize the mechanical properties of rocks (Xie et al. 2011). However, it is difficult to continuously capture the entire dynamic evolution process associated with the micro-mechanical behaviors in rocks in laboratory experiments using AE techniques (Lei et al. 2004). Additionally, although promising results have been achieved in the location of AE events, precise positioning of AE sources occurred in relatively small specimens remains challenging. Also, the source failure character cannot be completely obtained by AE monitoring due that the obtained signal may be easily perturbed by many factors such as material heterogeneity and natural fractures. Moreover, some AE events even possibly fail to be detected due to the limitation of monitoring equipment and the presence of background noises.

As a powerful complement to laboratory experiments, numerical simulations, owing to their rapidity, directness and convenience from the perspective of source mechanism interpretation, have been extensively employed to investigate the temporal and spatial distribution of AE events in

rock masses (Chong et al. 2017; Sun and Wu 2021; Zhang et al. 2020). Numerical methods can provide more detailed information on AE activities, such as local deformation, damage and fracture types, that are not directly available in physical experiment observations. Notably, the influence of every single parameter on the magnitude and spatial–temporal distribution of AE events can be effectively investigated in numerical simulations. Currently, the acquisition of AE information associated with the failure process of brittle rocks has been realized mainly based on three numerical approaches, i.e., finite element method (FEM), discrete element method (DEM) and combined finite-discrete element method (FDEM).

The numerical simulation of AE is first implemented in FEM using the continuum-based damage model, in which the fracturing behaviors are characterized by degrading the corresponding material properties of finite elements (such as strength or stiffness). A typical realization of this is found in the commercial FEM software package—Rock Failure Process Analysis (RFPA) (Tang 1997). In this approach, each damaged element is deemed as an AE event induced by the dissipation of elastic strain energy. Similar to this, other damage models, such as the local degradation model (Fang and Harrison 2002), elastoplastic cellular automata model (Feng et al. 2006) and local scalar damage model (Amitrano et al. 1999), have been developed to simulate AE activities associated with fracture propagation and coalescence from the perspective of energy release. However, FEM has difficulty in explicitly simulating the dynamic process of fracture nucleation and propagation. In addition, since the progressive failure in FEM is characterized by a heterogeneous distribution of rock mechanical parameters (weak discontinuities) rather than the real separation of physical surfaces (strong discontinuities), the energy release associated with AE activities cannot be well estimated and monitored, which may reduce the accuracy of AE simulations in FEM.

Compared with FEM, the DEM proposed by Cundall and Strack (1979) can explicitly simulate rock fragmentation, with remarkable advantages in analyzing fracture propagation regulations from the perspective of meso-mechanics without considering complex constitutive relations (Ferguen et al. 2019; Jiang et al. 2020). In recent years, the commercial PFC (Particle Flow Code) software developed based on DEM has broad applications in brittle rock related simulations (Castro-Filgueira et al. 2020; Xu and Cao 2018; Zhang and Zhang 2017). In PFC, each breakage of particle bond is regarded as a microcrack, and the particle kinetic energy upon bond breakage can be directly monitored to obtain the

microseismic energy radiated from the source. Hazzard and Young (2000) proposed a solution to simulate AE events in rock masses in PFC2D (2D PFC) based on kinetic energy release after bond breakage. In their model, each AE event may contain one or multiple microcracks, and they are realized by clustering bond breakages that occurred within a small spatial and temporal span, which makes the distribution of AE magnitude more realistic.

To further investigate the source mechanism of AE events, the moment tensor theory is also introduced in PFC according to the variation of contact force when bond breakage occurs (Hazzard and Young 2002). By decomposing the obtained moment tensor, the macroscopic fracture types (tensile or shear fractures) can be further distinguished (Zhang and Zhang 2017). In addition, the obtained moment tensor can provide supplementary information such as the geometric state of fractures (closed or open), which is not directly attainable from seismic wave data. However, since the rock matrix in PFC is represented by an assembly of rigid particles, its effectiveness in simulating the mechanical behaviors of compact crystalline rocks is arguable (Li et al. 2020). Additionally, due to the lack of highly interlocked grain structures, the particles could rotate after bond breakage, which lowers the brittleness of simulated rocks (Potyondy and Cundall 2004). Furthermore, because particle breakage occurs instantaneously without behaving strain-softening characters, the obtained magnitudes of AE are generally slightly larger (Hazzard and Young 2002). To compound matters, the determination of AE duration in PFC relies heavily on the imprecise empirical assumptions that each cluster with multiple microcracks is regarded as an expanded shear fracture (i.e., the influence of tensile fracture is inappropriately ignored) (Hazzard and Young 2000).

As an improvement, the combined finite-discrete element method (FDEM) (Munjiza et al. 2013), a state-of-the-art numerical approach that merges FEM-based analysis of continua with DEM-based contact processing for discontinua, is superior to both pure FEM and DEM, and thus can circumvent the deficiency of the aforementioned numerical approaches in simulating rock damage and failure. The FDEM can explicitly capture the dynamic fracturing process of rock masses. Its capability for characterizing rock failure processes from laboratory observations to engineering applications has been well validated in many aspects of rock mechanics in recent years, such as blasting (Han et al. 2020b; Wang et al. 2021a), discrete fracture network (Lei and Gao 2018; Lei et al. 2021), tunnel excavation (Han et al. 2020a), acoustic emission monitoring (Lisjak et al. 2013; Zhao et al. 2014, 2015) and multi-physical/field coupling (Yan et al. 2021, 2022).

Importantly, the seismic energy release can be explicitly evaluated in FDEM using quasi-dynamic techniques in the progressive fracturing process from continuum to discontinuum. Based on FDEM, Lisjak et al. (2013) proposed a means to simulate AE events by calculating the variation of kinetic energy from local damage to the complete breakage of cohesive elements. They investigated the relationships between the simulated seismicity and the deformation characteristics of a granite sample subjected to uniaxial compressive loading. On top of the AE simulation in FDEM, a non-parametric clustering algorithm is proposed by Zhao et al. (2014) to reduce the mesh dependency and to obtain more realistic seismic information associated with hydraulic fracturing. Recently, Zhao et al. (2023) further adopt the energy-based AE simulation to obtain a detailed comprehension of shear induced progressive damage and the associated seismic activity, and roughly evaluated the source mechanism by calculating a weighted average of each AE event. However, the energy-based AE simulation approach can only provide the distribution of AE event magnitude; it is difficult to capture the detailed deformation and motion of fracture sources and macro-fracturing types (Hazzard and Young 2002).

In this work, based on our 2D in-house FDEM code – Pamuco (**P**arallel · **m**ultiphysics · **c**oupling), we implement a moment tensor-based algorithm to simulate AE characteristics associated with fracture propagation and coalescence in brittle rocks. This approach not only can accurately capture the distribution of AE event magnitude, but also has the capability to further distinguish AE types and determine the geometric state (open or closed) of fractures. To the best of our knowledge, this is the first time the moment tensor-based approach for AE simulation has been realized in FDEM. The paper is organized as follows. In Sect. 2, we systematically introduce the fundamental principles of FDEM. In Sect. 3, by introducing the moment tensor theory, the AE model considering the clustering effect of microcracks is developed based on FDEM. In Sect. 4, we first establish a heterogeneous model to simulate the evolution of AE events under uniaxial compressive load, and verify the effectiveness of the developed approach for capturing the distribution of AE magnitude. Then, four typical tests are performed to validate the accuracy of the moment tensor-based approach in distinguishing the source mechanism of associated microcracks, and we revise the traditional criterion to better accommodate the identification of the full spectrum of AE source types. Following this, by decomposing the moment tensor, we investigate the types of macro-fracture containing multiple microcracks to demonstrate the appropriateness of the

proposed approach for simulating AE on the laboratory scale. We also analyze the failure mechanism of the rock bridge region between two pre-existing flaws at the end as an exemplar application of the implemented AE simulation approach. The conclusions are drawn in Sect. 5.

## 2 Fundamentals of FDEM

In this section, we first introduce the governing equation in FDEM. Then, the constitutive laws of cohesive elements for fracturing modeling are briefly presented. Finally, the contact algorithm between discrete elements is briefly introduced.

### 2.1 Governing Equation

In 2D FDEM models for rocks, the rock matrix is discretized into an assembly of triangle finite elements, and explicit time integration schemes are adopted to solve the motion equations for updating the displacement and velocity of nodes at each simulation time step. Generally, the governing equation in FDEM can be expressed as (Munjiza 2004)

$$\mathbf{M}\ddot{\mathbf{x}} + \mathbf{C}\dot{\mathbf{x}} = \mathbf{f}, \tag{1}$$

where  $\mathbf{M}$  is the mass matrix,  $\mathbf{C}$  is the damping matrix,  $\mathbf{x}$  is the node displacement vector, and  $\mathbf{f}$  represents the total force vector. The damping matrix is introduced to consume kinetic energy for quasi-static equilibrium cases, i.e., the so-called dynamic relaxation, which can be calculated by

$$\mathbf{C} = \eta\mathbf{I}, \tag{2}$$

where  $\eta$  and  $\mathbf{I}$  are the damping coefficient and identity matrices, respectively.

### 2.2 Rock Fracturing Modeling

As shown in Fig. 1a, rock failure is a progressive damage process where microcracks are first initiated from fracture tips, and gradually develop into meso- or macro-fractures. To simulate fracture initiation and propagation in rocks, four-node zero-thickness cohesive elements are inserted between adjacent triangle finite elements before the onset of simulation to capture the progressive fracturing process (see Fig. 1b, c). The stress of each cohesive element is calculated based on the relative displacement and geometric position of its two edges associated with the two neighboring finite elements. At present, the fracturing modes of cohesive elements mainly consider three types, i.e., Mode I (tensile fracturing), Mode II (shear fracturing), and mixed Mode I–II (tensile-shear mixed fracturing).

Figure 2 presents the constitutive laws of cohesive element for the three fracturing modes, where  $o$  and  $l|s|$  respectively represent the relative opening and slipping displacement of cohesive element induced by the relative motion of adjacent triangular elements;  $o_p$  and  $s_p$  are the elastic limits of  $o$  and  $l|s|$ , respectively;  $o_t$  and  $s_t$  are the critical values of  $o$  and  $l|s|$ , respectively;  $T_s$  is the tensile strength of cohesive element;  $c$  and  $\varphi$  denote the cohesion and internal friction angle of cohesive element, respectively. As shown in Fig. 2b, when the normal opening  $o$  increases to the elastic limits  $o_p$ , the normal cohesive stress ( $\sigma^{\text{coh}}$ , tensile positive) reaches the tensile strength  $T_s$ , which marks the damage initiation point of cohesive element; as  $o$  continues to increase, the cohesive element starts to damage, i.e., enters the strain-softening stage, and  $\sigma^{\text{coh}}$  gradually decreases in a nonlinear manner; when  $o$  reaches the critical (maximum) normal opening  $o_t$ , i.e., the breakage point (complete damage) of cohesive element, a pure tensile microcrack will be generated (Mode I). Similarly, as presented in Fig. 2c, the shear cohesive stress ( $\tau^{\text{coh}}$ ) reaches the critical value ( $\tau^{\text{coh}} = c - \sigma^{\text{coh}} \tan \varphi$ ) when the tangential slipping  $l|s|$  increases to the elastic limits  $s_p$  (cohesive damage

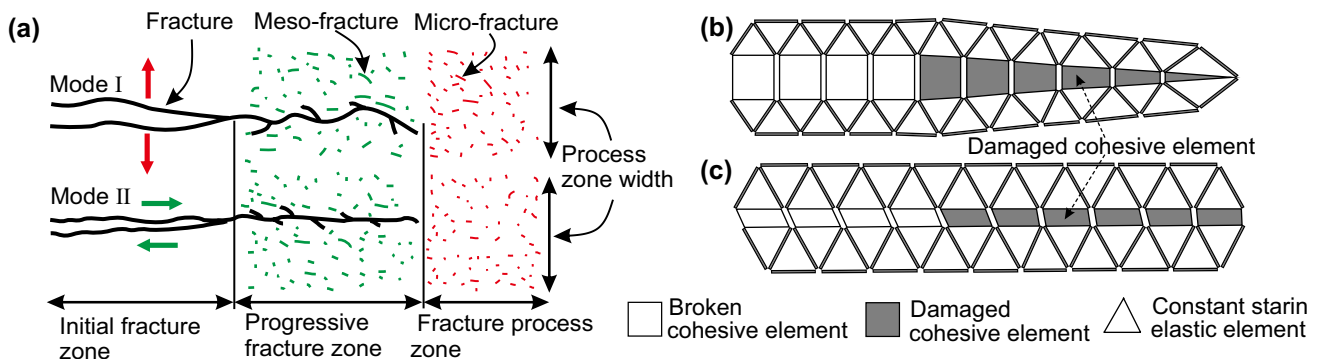


**Fig. 1** Fracturing modeling strategy in FDEM. (a) Schematic of fracture process zone (FPZ) development ahead of a fracture tip (modified from Mohammadnejad et al. 2018). Schematic of FDEM model

consisting of triangular elements connected by cohesive elements to simulate (b) Mode I and (c) Mode II fractures, respectively

initiation point); in contrast to the normal cohesive stress,  $\tau^{\text{coh}}$  reaches the residual value at  $|\sigma^{\text{coh}} \tan \varphi|$  rather than zero when the normal cohesive stress is negative (compressive); the pure shear microcrack (Mode II) is generated when the tangential slipping reaches the maximum value  $s_t$  (cohesive breakage point). Note that here the Mohr–Coulomb criterion is adopted to determine the shear strength (i.e., the peak shear stress in Fig. 2c). The cohesive element breakage of mixed Mode I–II is determined by the joint effect of normal opening and tangential slipping (Fig. 2d). Specifically, the newly generated microcrack could be deemed as mixed Mode I–II if  $o$  and  $|s|$  satisfy the condition of

$$\sqrt{\left(\frac{o - o_p}{o_t - o_p}\right)^2 + \left(\frac{|s| - s_p}{s_t - s_p}\right)^2} \geq 1. \quad (3)$$

It is worth emphasizing that in the present paper the term “microcrack” is specially preserved to denote the breakage of a single cohesive element.

The normal and shear cohesive stress ( $\sigma^{\text{coh}}$  and  $\tau^{\text{coh}}$ ) can be, respectively, calculated by Eqs. (4) and (5), which fully consider the tensile and shear softening behaviors (Fukuda et al. 2019a, b):

$$\sigma^{\text{coh}} = \begin{cases} \frac{2o}{o_{\text{lap}}} T_s & \text{if } o < 0 \\ \left[ \frac{2o}{o_p} - \left(\frac{o}{o_p}\right)^2 \right] f(D) T_s & \text{if } 0 \leq o \leq o_p, \\ f(D) T_s & \text{if } o > o_p \end{cases}, \quad (4)$$

$$\tau^{\text{coh}} = \begin{cases} f(D)c & \text{if } \sigma^{\text{coh}} > 0, |s| \geq s_p \\ \left[ \frac{2|s|}{s_p} - \left(\frac{|s|}{s_p}\right)^2 \right] f(D)c & \text{if } \sigma^{\text{coh}} > 0, 0 < |s| < s_p \\ \left[ \frac{2|s|}{s_p} - \left(\frac{|s|}{s_p}\right)^2 \right] (f(D)c - \sigma^{\text{coh}} \tan \varphi) & \text{if } \sigma^{\text{coh}} < 0, 0 < |s| < s_p \\ f(D)c - \sigma^{\text{coh}} \tan \varphi & \text{if } \sigma^{\text{coh}} < 0, |s| \geq s_p \end{cases}. \quad (5)$$

Here,  $o_{\text{lap}}$  is the overlap distance of adjacent triangular finite elements when  $o$  is negative. The function  $f(D)$  is crucial to characterize the strain-softening behavior of cohesive elements based on a damage coefficient  $D$  (Tatone and Grasselli 2015), i.e.,

$$f(D) = \left[ 1 - \frac{a+b-1}{a+b} \exp\left(D \frac{a+cb}{(a+b)(1-a-b)}\right) \right] \times [a(1-D) + b(1-D)^c] \quad (0 \leq D \leq 1), \quad (6)$$

where  $a$ ,  $b$  and  $c$  are intrinsic rock properties that determine the shapes of the softening curves shown in Fig. 2b, c. The value of  $D$ , ranging from 0 to 1, for Mode I, Mode II, and mixed Mode I–II can be, respectively, obtained by

$$D = \frac{o - o_p}{o_t - o_p}, \quad (7)$$

$$D = \frac{|s| - s_p}{s_t - s_p}, \quad (8)$$

and

$$D = \sqrt{\left(\frac{o - o_p}{o_t - o_p}\right)^2 + \left(\frac{|s| - s_p}{s_t - s_p}\right)^2}. \quad (9)$$

Generally, the microcrack type can be categorized as tensile, shear, or mixed when cohesive element breakage occurs. In this work, we define the term “damage type” ( $D_i$ ), ranging from 0 to 1, to characterize the microcrack type by normalizing the shear and tensile displacements, i.e.,

$$D_i = \max\left(\frac{o}{\sqrt{o^2 + |s|^2}}, 0\right), \quad (10)$$

where 0 represents pure shear type, 1 represents pure tensile type, and others indicate the mixed type. The fracture energy  $G_{f1}$  and  $G_{f2}$  of Mode I and Mode II are, respectively, given by (Fukuda et al. 2019a, b)

$$G_{f1} = \int_{o_p}^{o_t} \sigma^{\text{coh}}(o) do, \quad (11)$$

and

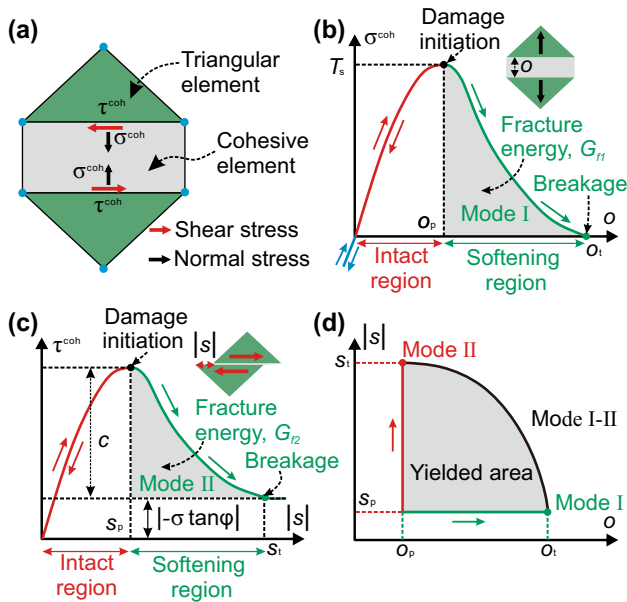


**Fig. 2** Constitutive laws of cohesive elements. (a) Assembly of a cohesive element. (b) Constitutive of tensile fracturing mode, i.e., Mode I. (c) Constitutive of shear fracturing mode, i.e., Mode II. (d) Constitutive of mixed fracturing mode, i.e., mixed Mode I–II. Here,  $o$  and  $|s|$  represent the relative opening and slipping displacement of a cohesive element, respectively;  $o_p$  and  $s_p$  are the elastic limits of  $o$  and  $|s|$ , respectively;  $o_t$  and  $s_t$  are the critical values of  $o$  and  $|s|$ , respectively;  $T_s$  is the tensile strength of cohesive element;  $c$  and  $\varphi$  denote the cohesion and internal friction angle of a cohesive element, respectively;  $G_{f1}$  and  $G_{f2}$  are the fracture energy of Mode I and II, respectively

$$G_{f2} + W_{res} = \int_{s_p}^{s_t} \{ \tau^{coh} |s| \} d|s|, \tag{12}$$

which correspond to the areas under the curves in Fig. 2b and c in the softening regions, respectively. Here,  $W_{res}$  is the amount of work per area that has been done by the residual stress in Mohr–Coulomb shear strength model.

### 2.3 Contact Algorithm

The contact algorithm for processing the interaction between neighboring finite elements in FDEM involves contact detection and contact interaction. The contact detection of elements in touch is conducted to determine contact couples (the two corresponding elements are denoted as contactor and target, respectively) using the efficient NBS (non-binary search) algorithm which yields a theoretical CPU time proportional to the total number of finite elements (Munjiza and Andrews 1998). After obtaining the contact couples, the contact interaction algorithm will be invoked to calculate the contact forces. The normal contact force is calculated based on the overlap area of contact couples, while the tangential contact force is determined by their relative slipping displacement; both are performed in a penalty-based manner. More details regarding the formulations of normal and tangential contact forces are available in previous works (Munjiza 2004; Munjiza et al. 2011; Tatone and Grasselli 2015).

### 3 Moment Tensor-Based AE Simulation Approach in FDEM

In this section, first, a clustering algorithm is implemented to combine multiple microcracks that occurred close in space and time as a distinct AE event. Then, we introduce the concept of moment tensor to characterize AE events in FDEM. Finally, two typical means for distinguishing fracture types are presented by decomposing the obtained moment tensor. For clear reference, in the subsequent text, an AE event indicates a cluster of one or more cohesive element breakages (i.e., a cluster of microcracks) that have been combined using the clustering algorithm, and the term “macro-fracture” denotes the fracture generated associated with an AE event.

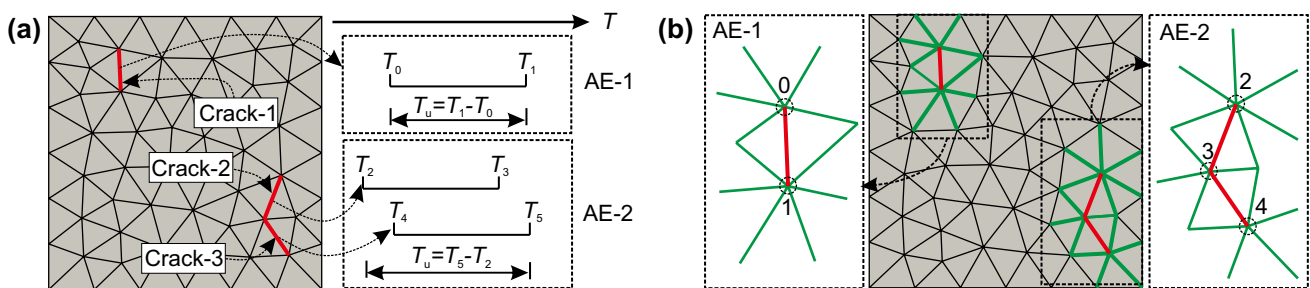


**Fig. 3** (a) Duration time and (b) source area of an AE event. AE-1 and AE-2 denote the two AE events; Crack-1, Crack-2 and Crack-3 represent the three involved microcracks (marked in red lines); the element edges in the source area of an AE event are marked in green.

Here, AE-1 only contains Crack-1, and AE-2 consists of Crack-2 and Crack-3.  $T_i$  represents the damage initiation time or breakage time of the cohesive elements related to the three microcracks, and  $T_u$  denotes the duration time of an AE event

### 3.1 Formulations of an AE Event

It is common that an AE event may involve multiple microcracks (Liu et al. 2018; Scholz 2019). To appropriately capture and define AE events in FDEM, we propose a clustering algorithm to combine microcracks that are spatially and temporally connected. Note that a similar clustering algorithm has been proposed in previous works using a non-parametric Gaussian kernel density estimation (Zhao 2017; Zhao et al. 2014, 2023). Beforehand, it is necessary to define the basic concepts such as duration time and source area of an AE event. As illustrated in Fig. 3a, there are three generated microcracks, i.e., Crack-1, Crack-2 and Crack-3, and the damage initiation time and breakage time of the three corresponding cohesive elements are, respectively, indicated by the time scale bars presented on the right-hand side. We combine the microcracks having spatial connection as well as temporal overlap in terms of cohesive softening stage, and form two AE events, i.e., AE-1 and AE-2, which, respectively, contain one (Crack-1) and two microcracks (Crack-2 and Crack-3). For AE-1, its duration time can be obtained by the difference between the damage initiation time and the

breakage time of the cohesive element related to Crack-1, i.e.,  $T_u = T_1 - T_0$ . While for AE-2, since Crack-2 and Crack-3 emerge successively, the duration time is represented by the difference between the damage initiation time of the cohesive element corresponding to the first generated microcrack (i.e., Crack-2) and the breakage time of the cohesive element corresponding to the last generated microcrack (i.e., Crack-3), i.e.,  $T_u = T_5 - T_2$ .

Note that the duration time of an AE event generally spans several computation time steps, and we conduct the above clustering algorithm in each time step. For convenience, the terms “active” and “inactive” are utilized to describe the status of an AE event: “active” denotes that one or several involved cohesive elements in an AE event are still in the softening stage (i.e., have not reached the final breakage point yet), and thus other microcracks are still possible to be combined into this AE event; “inactive” indicates that all the involved cohesive elements of an AE event have passed their breakage point and thus no other microcracks can be further combined into this AE event, which marks the completeness of an AE event. For the example shown in Fig. 3a, AE-1 or AE-2 are active during the time  $T_0$  and  $T_1$ , and  $T_2$  and  $T_5$ , respectively. The source area of an AE event can be demonstrated in Fig. 3b, in which the microcracks contained in each AE event are marked in red, the edges of the related triangular finite elements in the source area of an AE event are marked in green, and those edges are connected by common nodes. For example, all finite element edges connected to nodes 0 and 1 are regarded as within the source area of AE-1; likewise, all finite element edges related to nodes 2, 3 and 4 are deemed as located in the source area of AE-2.

The determination of the radius of an AE event can still be demonstrated based on the two aforementioned AE events – AE-1 or AE-2, as is presented in Fig. 4. The center of an AE event is determined by the geometric center of all microcracks it contains, which can be calculated by averaging the coordinates of all nodes of involved microcracks, i.e.,

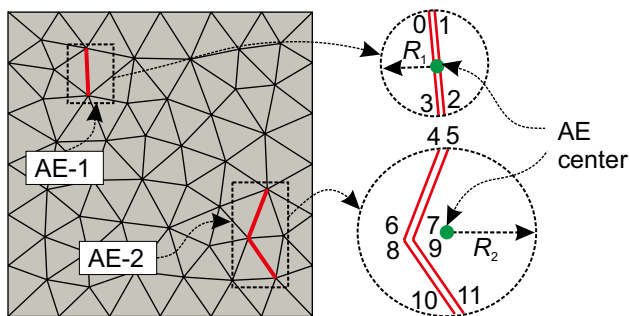


**Fig. 4** The radius of an AE event. Microcracks are marked in red, and AE centers are denoted by green dots. AE-1 and AE-2 denote the two AE events, in which AE-1 contains one microcrack and AE-2 consists of two microcracks.  $R_1$  and  $R_2$  are the radii of AE-1 and AE-2, respectively

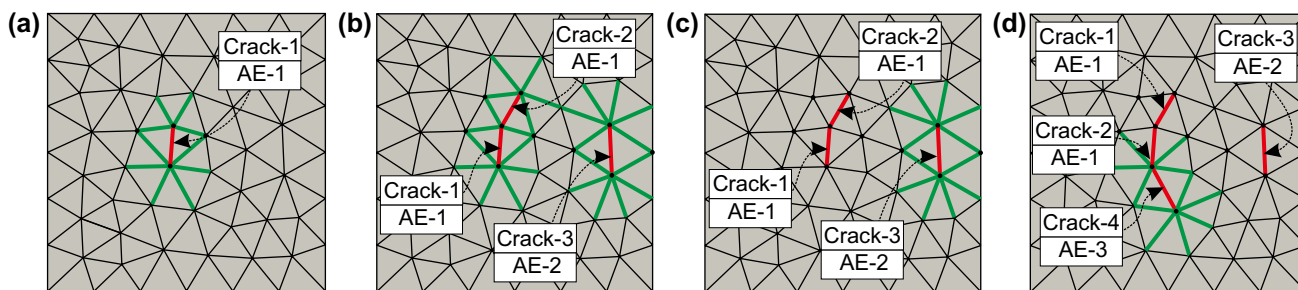


**Fig. 5** Evolution of AE events at four consecutive timestamps: (a)  $T_0$ . (b)  $T_1$ . (c)  $T_2$ . (d)  $T_3$ . Crack-1, Crack-2, Crack-3 and Crack-4 represent the four successive microcracks induced by cohesive element breakage. AE-1, AE-2 and AE-3 denote the three AE events formed based

on the four microcracks. The microcracks are marked in red, and the finite element edges in the source area of AE events are marked in green

$$\begin{cases} \bar{x} = \frac{1}{n} \sum_{i=1}^n x_i \\ \bar{y} = \frac{1}{n} \sum_{i=1}^n y_i \end{cases}, \quad (13)$$

where  $x_i$  and  $y_i$  ( $i = 1, 2, \dots, n$ ) are, respectively, the  $x$  and  $y$  coordinates of each node;  $\bar{x}$  and  $\bar{y}$  denote the coordinates of AE event center. Then, the radius  $R$  of an AE event is the maximum distance from the nodes of each involved microcrack to the AE event center, i.e.,

$$R = \max_{i \in (1, n)} \left( \sqrt{(\bar{x} - x_i)^2 + (\bar{y} - y_i)^2} \right), \quad (14)$$

Although the center of an AE event is determined by stress “glut” (the distribution of inelastic stresses) (Backus 1977), this geometrical center calculation approach of AE events usually produces satisfactory results (Hazzard and Young 2002).

We use a specially designed example shown in Fig. 5 to illustrate the formation and evolution of AE events in our proposed AE simulation approach, where Crack-1, Crack-2, Crack-3 and Crack-4 represent the four microcracks (marked in red) generated successively, and AE-1, AE-2 and AE-3 denote the three AE events formed based on the four microcracks. The edges of finite elements located in the source areas of AE events are marked in green. The detailed realization of AE event simulation in FDEM using the clustering algorithm of connected microcracks is demonstrated as follows:

- a. First, the cohesive element corresponding to Crack-1 reaches the damage initiation point at time  $T_0$  (Fig. 5a),

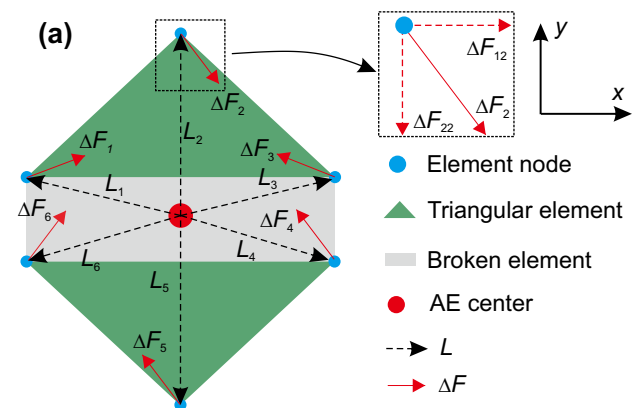
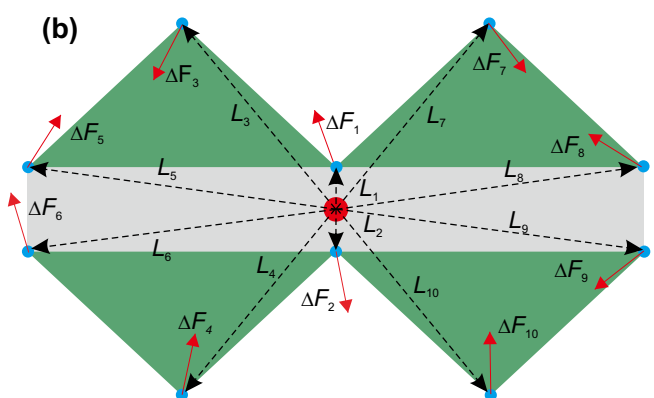


**Fig. 6** Schematic of moment tensor calculation for AE events containing (a) one microcrack or (b) multiple microcracks.  $\Delta F$  and  $L$  denote the vector of node force change and the distance from a node to the AE center, respectively. The vector of node force change and

- which is deemed as the starting time of AE-1 and the status of AE-1 is marked as “active”.
- b. As the model evolves to time  $T_1$  (Fig. 5b), another two cohesive elements corresponding to Crack-2 and Crack-3, respectively, reach the damage initiation point. Since the cohesive element of Crack-2 lies in the source area of AE-1, and we assume that the status of AE-1 is still active at this time, i.e., the softening stage of this cohesive element overlaps that of AE-1, Crack-2 will be combined into AE-1. Then the radius and location of AE-1 need to be updated accordingly, while its duration time ( $T_u$ ) can only be determined later when the last involved cohesive element reaches the breakage point. However, the cohesive element of Crack-3 is apparently out of the source area of AE-1, and it will be regarded as a new AE-2 and marked as “active”.
- c. The model then evolves to time  $T_2$  (Fig. 5c) when the last cohesive element in AE-1 reaches the breakage point. The status of AE-1 is changed to “inactive”, and its duration time is calculated as  $T_u = T_2 - T_0$ . Meanwhile, the moment tensor and magnitude of AE-1 are calculated based on the equations shown later in the next section.
- d. The model continues to evolve to time  $T_3$  when a new cohesive element corresponding to Crack-4 reaches the damage initiation point (Fig. 5d). Although Crack-4 is located in the source area of the previous event AE-1, it cannot be combined into AE-1 since the status of AE-1 is “inactive”. Thus, a new active AE event—AE-3—needs to be marked. Assuming that the cohesive element corresponding to Crack-3 reaches the breakage point at a time somewhere between  $T_1$  and  $T_3$ , similar to AE-1, the status of AE-2 is supposed to be changed to “inactive” and its moment tensor and magnitude need to be calculated at that specific time step.



the distance can be further decomposed into components along the  $x$  and  $y$  axis, which correspond to the components of  $\Delta F_{ik}$  and  $L_{kj}$  in Eq. (15)

In the above example, AE-1 contains two microcracks (Crack-1 and Crack-2), while AE-2 and AE-3 only have one microcrack (Crack-3 and Crack-4, respectively), i.e., each AE event may contain one or more microcracks. In FDEM, the clustered microcracks in each AE event are stored in a linked list according to their occurrence orders, and the list is dynamically updated when new cohesive elements enter the softening stage.

### 3.2 Moment Tensor of an AE Event

The nodal force and location of each node are updated at each time step in FDEM. When an AE event is finalized, i.e., marked as “inactive”, its moment tensor can be calculated based on the changes in nodal forces and node locations of each involved cohesive element during the softening stage. For example, for an AE event containing only a single microcrack (Fig. 6a), when the corresponding cohesive element evolves from the damage initiation point to the breakage point, the nodal forces of the source triangular elements will witness a progressive change. Then, the moment tensor of this AE event can be calculated based on the changes in node locations and nodal forces using (Hazzard and Young 2002)

$$\mathbf{M}_{ij} = \Delta \mathbf{F}_{ik} \mathbf{L}_{kj}, \quad (15)$$

where  $\Delta \mathbf{F}_{ik}$  represents the components of nodal force change of each node, which can be obtained by subtracting the nodal force at the damage initiation point from the breakage point;  $\mathbf{L}_{kj}$  is the components of distance measured from each node to the AE event center; the subscripts  $i$  and  $j$  correspond to the dimension of the model, i.e.,  $i, j = 1, 2$  for 2D cases; the subscript  $k$  denotes the number of nodes located in the source area of AE event. Note that the node force change for each cohesive element is recorded when it reaches the breakage point. If an AE event contains multiple microcracks (e.g., Fig. 6b), we can still calculate the moment tensor using Eq. (15), with the only difference that we need to update the AE center using Eq. (13) by considering all the involved cohesive elements.

It is worth noting that the definition of AE source area has influence on the calculated AE event magnitude, albeit the influence is minor according to our comparison (not shown here due to space limitation). By considering the computational expense, we only take into account the force changes on the nodes around the broken cohesive crack elements in this work. The influence of various definitions of source area on AE magnitude distribution will be reported in the future.

Similar to the kinetic energy-based AE simulation approach proposed earlier (Hazzard and Young 2000; Lisjak et al. 2013), the moment tensor-based AE simulation

approach implemented here can also effectively characterize the AE magnitude. According to the scalar moment, the magnitude  $M_w$  of an AE event can be estimated by (Hanks and Kanamori 1979)

$$M_w = \frac{2}{3} \log M_0 - 6, \quad (16)$$

Here (Silver and Jordan 1982)

$$M_0 = \sqrt{0.5 \times \sum_{j=1}^2 m_j^2}, \quad (17)$$

where  $m_j$  ( $j = 1, 2$ ) is the eigenvalue of the moment tensor, and  $M_0$  is the scalar moment.

### 3.3 Moment Tensor Decomposition Approaches

In addition to AE event magnitude, the proposed technique can also provide more information such as the deformation and motion type of AE sources by decomposing the obtained moment tensor. Since the moment tensor is a symmetric matrix, it can be diagonalized and decomposed into the following parts (Chong et al. 2017):

$$\mathbf{M} = \mathbf{M}^{\text{ISO}} + \mathbf{M}^{\text{CLVD}} + \mathbf{M}^{\text{DC}}, \quad (18)$$

where  $\mathbf{M}^{\text{ISO}}$  is the isotropic part (ISO),  $\mathbf{M}^{\text{CLVD}}$  is the compensated linear vector dipole (CLVD), and  $\mathbf{M}^{\text{DC}}$  is the double-couple (DC) part. In seismology practice, the relative scalar factors  $C_{\text{ISO}}$ ,  $C_{\text{CLVD}}$  and  $C_{\text{DC}}$  of a seismic event are utilized to, respectively, quantify the proportion of ISO, DC and CLVD parts in the moment tensor (Vavryčuk 2014). Here,  $C_{\text{ISO}}$  indicates the isotropic volumetric change in an AE source, where positive values represent tensile opening and negative represent compressive closure; the  $C_{\text{CLVD}}$  denotes some compensated strain component from an AE source, and  $C_{\text{DC}}$  characterizes the relative motion trend from two vector pairs with equal magnitude but opposite directions (Martínez-Garzón et al. 2017). The three scalar factors are given in 3D space (Vavryčuk 2014)

$$C_{\text{ISO}} = \frac{M_1 + M_2 + M_3}{|M_1 + M_2 + M_3| + M_1 - M_3}, \quad (19)$$

$$C_{\text{CLVD}} = \frac{M_1 + M_3 - 2M_2}{|M_1 + M_2 + M_3| + M_1 - M_3}, \quad (20)$$

and

$$C_{\text{DC}} = \frac{M_1 - M_3 - |M_1 + M_3 - 2M_2|}{|M_1 + M_2 + M_3| + M_1 - M_3}, \quad (21)$$

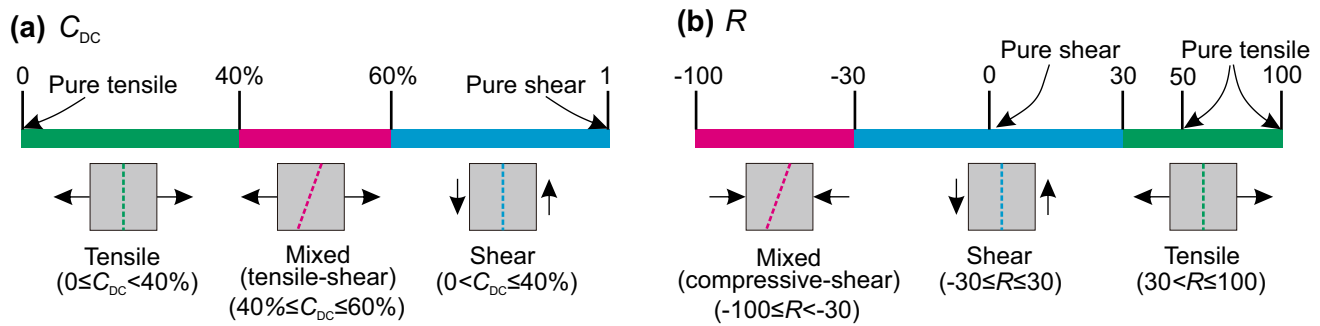


**Fig. 7** Classification criteria of the source type of AE events based on (a)  $C_{DC}$  and (b)  $R$

where  $M_1$ ,  $M_2$  and  $M_3$  are the real eigenvalues of the moment tensor and we usually define  $M_1 \geq M_2 \geq M_3$ . For 2D cases, we only have two eigenvalues and the third one is assumed zero. Here, the scalar factors  $C_{ISO}$ ,  $C_{CLVD}$  and  $C_{DC}$  satisfy (Vavryčuk 2014)

$$|C_{ISO}| + |C_{CLVD}| + C_{DC} = 1, \quad (22)$$

The  $C_{ISO}$  and  $C_{CLVD}$  range from -1 to 1, and  $C_{DC}$  is always positive from 0 to 1 (Vavryčuk 2014). Based on  $C_{DC}$ , an AE event can be classified as having a tensile source if  $C_{DC} < 40\%$ , a mixed source if  $40\% \leq C_{DC} \leq 60\%$ , and a shear source if  $C_{DC} > 60\%$ ; particularly,  $C_{DC} = 0$  and 1, respectively, correspond to pure tensile and pure shear AE source (Ohtsu 1995).

In addition, Feignier and Young (1992) proposed another approach to quantify the failure mechanism of AE events and distinguish the macro-fracture types by decomposing the moment tensor into isotropic and deviatoric parts. The variable  $R$ , the ratio of the isotropic to the deviatoric component of the moment tensor, is given by

$$R = \frac{100 \times \text{tr}(\mathbf{M})}{|\text{tr}(\mathbf{M})| + \sum_{i=1}^2 |m_i^*|}, \quad (23)$$

Here,  $\text{tr}(\mathbf{M})$  denotes the trace of the moment tensor, i.e.,  $\text{tr}(\mathbf{M}) = \sum m_i$  ( $i = 1, 2$  for 2D cases) and  $m_i$  represents the eigenvalue of the moment tensor;  $m_i^* = m_i - \text{tr}(\mathbf{M})/2$ . The  $R$  ranges from -100 to 100: a tensile AE event occurs if  $R > 30$ , a mixed event (compressive-shear) if  $R < -30$ , and a shear event if  $-30 \leq R \leq 30$ . Especially,  $R = 0$  and 100, respectively, correspond to pure shear and pure tensile (biaxial tensile loading) AE sources (Zhang and Zhang 2019). Note that  $R = 50$ , corresponding to an AE event occurred under uniaxial tensile loading, also indicates a pure tensile AE source (Zhao et al. 2021). The classification criteria of AE source types based on DC and  $R$  are sketched in Fig. 7. For convenience, the two above-mentioned methods for

distinguishing AE source types based on  $C_{DC}$  component and variable  $R$  are abbreviated as Cra-DC and Cra-R, respectively. It is also worth mentioning that the mixed AE source type which can be directly identified in Cra-DC and Cra-R are, respectively, of tensile-shear mixed and compressive-shear mixed. Hence, we suspect that Cra-DC and Cra-R may be incapable of straightforwardly identifying the compressive-shear mixed and tensile-shear mixed AE source types, respectively (Jost and Herrmann 1989; Vavryčuk 2014). The effectiveness and applicability of these two methods will be discussed in Sect. 4.2 based on the proposed moment tensor-based AE simulation approach in FDEM.

## 4 Validations and Exemplar Applications

In this section, a heterogeneous rock model is first established to verify the effectiveness of the proposed moment tensor-based AE simulation approach in FDEM in terms of the distribution of AE event magnitude. Subsequently, four typical models are performed to validate the accuracy

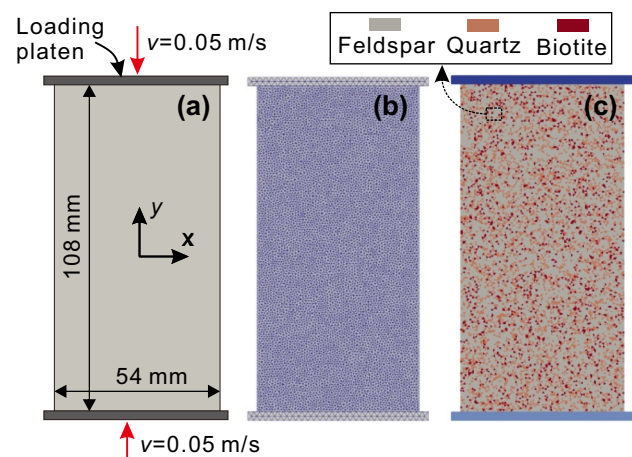


**Fig. 8** Model for uniaxial compression tests. (a) Model geometry. (b) Mesh result. (c) Mineral distribution

of the proposed AE simulation approach in distinguishing AE source types on microscale. Furthermore, the criterion for distinguishing fracture types is improved to accommodate the identification of the full-spectrum AE source types. Finally, based on moment tensor decomposition, we discuss the capability of the moment tensor-based approach for distinguishing macro-fracture types on laboratory scale, and give an exemplar application of the implemented AE simulation approach by analyzing the failure mechanism of a rock bridge region between two pre-existing flaws in a rock specimen subjected to uniaxial compressive loads.

**Table 1** Mineral properties for uniaxial compression simulations (adapted from Abdelaziz et al. 2018; Lisjak et al. 2013)

Input parameters (unit)	Feldspar	Quartz	Biotite
Volume fraction of minerals	71%	21%	8%
Young's modulus, $E$ (GPa)	56.4	83.1	17.2
Bulk density, $\rho$ (kg/m <sup>3</sup> )	2600	2600	2700
Poisson's ratio, $\nu$	0.32	0.07	0.36
Tensile strength, $f_t$ (MPa)	5.5	11.4	4.2
Cohesion, $c$ (MPa)	24.2	24.2	24.2
Internal friction angle, $\phi$ (°)	51.8	51.8	51.8
Mode I fracture energy, $G_{I1}$ (J/m <sup>2</sup> )	310	907	599
Mode II fracture energy, $G_{I2}$ (J/m <sup>2</sup> )	620	1814	1198
Normal contact penalty, $P_n$ (GPa)	56.4	83.1	17.2
Tangential contact penalty, $P_s$ (GPa)	564	831	172
Cohesive penalty, $P_f$ (GPa)	282	416	86
Sample-platen friction coefficient, $k_1$ (–)	0.1	0.1	0.1
Sample friction coefficient, $k_2$ (–)	0.7	0.7	0.7

## 4.1 Validation for AE Magnitude Distribution

To validate the effectiveness of the proposed moment tensor-based AE simulation approach in capturing AE event magnitude, a series of uniaxial compression tests are conducted, in which the width and height of the specimen are 54 mm and 108 mm, respectively (see Fig. 8a). The numerical model is discretized into 17,182 unstructured triangular elements with a mesh size of 0.95 mm using the Delaunay meshing scheme (Fig. 8b), which meets the requirement of mesh size for such simulation (Tatone and Grasselli 2015). The axial loads are imposed on the specimen through two rigid platens moving in opposite directions at a constant velocity of 0.05 m/s. The selection of the loading rate fully considers the effect of element size and ensures an acceptable running time. Although the loading velocity is larger than that in physical experiments, the mechanical response of the specimen would not be influenced notably (Mahabadi et al. 2012; Tatone and Grasselli 2015).

It should be noted that a pure homogeneous model is difficult to produce localized cohesive element breakages (i.e., AE events) before axial stress reaches 70–80% of the peak axial stress (Lisjak et al. 2013). This may bias the distribution of AE event magnitude compared with that of physical experiments, given that natural rocks are generally heterogeneous. Hence, a heterogeneous model is adopted here, similar to that in other AE simulations (Lisjak et al. 2013; Zhao et al. 2015), in which the rock is composed of 71% feldspar, 21% quartz and 8% biotite (see Fig. 8c). The physical–mechanical properties of each mineral are summarized in Table 1, which has been well calibrated in previous literature (Abdelaziz et al. 2018; Lisjak et al.

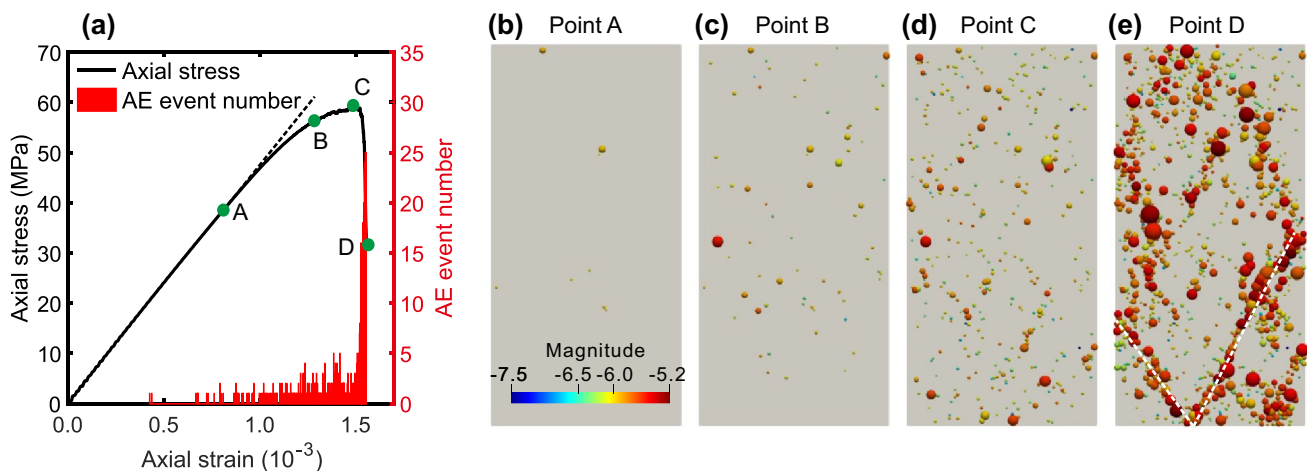


**Fig. 9** (a) Axial stress and AE event number versus axial strain. The distribution of AE event magnitude at the four loading points on the stress–strain curve: (b) point A, (c) point B, (d) point C and (e) point D. The corresponding axial stresses at points A, B, C, and D (i.e., green dots in a) are 38.25 MPa, 54.84 MPa, 58.85 MPa and

31.17 MPa, respectively. The size of the dots in b–e denotes the radius of AE events, and the color represents the magnitudes (estimated by Eq. (16)). The throughgoing macroscopic fracture planes are highlighted by white dashed lines in Fig. 9d

2013). To realize the more realistic weak interfaces between different minerals, the Mode I fracture energy,  $G_{f1}$ , for the interfaces between biotite and feldspar, between biotite and quartz, as well as between quartz and feldspar are reduced to 0.05, 0.05 and 0.6 J/m<sup>2</sup>, respectively. Other properties, such as the Mode II fracture energy ( $G_{f2}$ ), cohesive element penalty ( $P_f$ ), contact penalty ( $P_n$ ,  $P_s$ ) and internal friction angle ( $\phi$ ) at mineral interfaces are assigned with the average values of the two minerals along the two sides of the interfaces.

The axial stress and AE event number versus axial strain are presented in Fig. 9a. We select four typical turning points on the stress–strain curve, i.e., points A, B, C, and D, corresponding to the axial stress of 38.25 MPa, 54.84 MPa, 58.85 MPa and 31.17 MPa, respectively, to demonstrate the evolution of simulated AE events. Note that the selection of these points is based on the variation on the stress–strain curve, where an evident change in the number of generated AE events can be observed. At point A, i.e., the transition point of the stress–strain curve from linear to non-linear, only very few AE events can be observed (Fig. 9b). When the axial stress increases to point B, more AE events have occurred and more damages have been accumulated (Fig. 9c), which results in an apparent nonlinear behavior on the stress–strain curve. As the model loaded to peak stress at point C, the occurrence of AE events is more frequent due to the large number of initiated microcracks. Meanwhile, the AE events are pervasively distributed in almost all locations in the specimen (Fig. 9d). It can be observed that prior to the peak stress (e.g., points A to C), the occurrences of AE events are mainly induced by the cohesive element breakages at weaker interfaces between biotite-feldspar and biotite-quartz, which dominates the nonlinear behavior on the stress–strain curve. Additionally, the locations of AE events are mainly random and no obvious macroscopic fracture plane is formed, in which the magnitude of AE events mainly distributes in a range between  $-7.5$  and  $-6.0$ , indicating that the radiated energy of AE events is relatively small before the peak stress. As the axial strain continues to increase, the axial stress quickly drops to point D, and the number of AE events experiences a sharp surge, which manifests a typical failure behavior of brittle rocks. Throughgoing macroscopic fracture planes are formed and extended from the bottom to both sides of the specimen (see white dotted lines in Fig. 9e). It can be seen that AE events with large magnitudes (e.g., from  $-6.0$  to  $-5.2$ ) mainly occur after the peak stress due to the constant propagation and coalescence of microcracks, which is consistent with the previous observations (Lisjak et al. 2013; Liu et al. 2018).

To further investigate the relationship between AE magnitude distribution and the axial strain of the specimen, the Gutenberg-Richter relation is adopted to estimate the

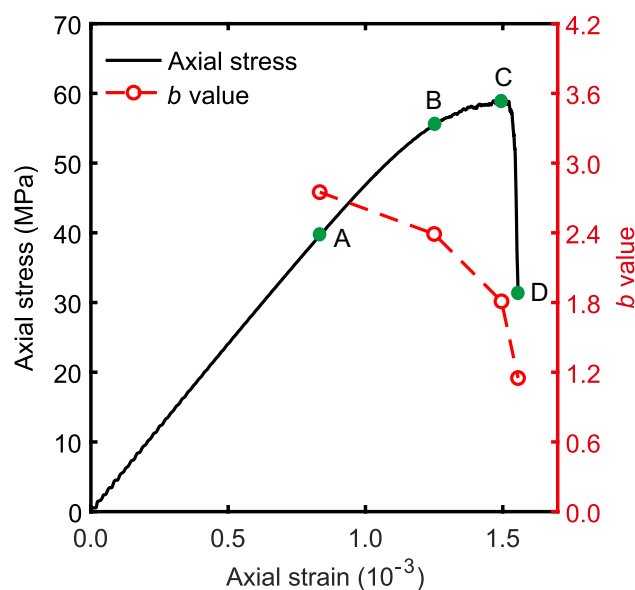


**Fig. 10** Axial stress and  $b$  value versus axial strain. The points A, B, C and D correspond to that in Fig. 9a

frequency-magnitude distribution of the simulated AE events, which is given by (Gutenberg and Richter 1942)

$$\log N(> M_w) = a - bM_w. \quad (24)$$

where  $M_w$  denotes the magnitude of AE event,  $N$  is the number of AE events with a magnitude greater than  $M_w$ , and  $a$  and  $b$  are constants. The  $b$  value is estimated using the maximum likelihood method (MLM) proposed in previous works (Aki 1965; He et al. 2018; Woessner and Wiemer 2005; Zhao et al. 2015). Generally, lower  $b$  values represent high energy dissipation accompanied by faster fracture growth (Lisjak et al. 2013; Liu et al. 2018). As presented in Fig. 10, the  $b$  values at the four points A, B, C and D are 2.75, 2.38, 1.81 and 1.15, respectively, i.e., the  $b$  value gradually decreases with the increase of axial strain, which corresponds to the fracturing evolution process from the initiation and propagation of microcracks to the formation of throughgoing macroscopic fracture planes (Liu et al. 2018). Specifically, prior to the peak stress, the  $b$  value decreases linearly from 2.75 to 1.81, and the number of AE events witnesses a steady increase (see Fig. 9a), indicating that a stable variation of  $b$  value corresponds to the initiation of microcracks. After the peak stress, the  $b$  value decreases sharply from 1.81 to 1.15, which is consistent with the rapid stress drop accompanied by a large number of propagation and coalescence of microcracks shown in Fig. 9d. This demonstrates that the  $b$  value can not only characterize the process of fracturing and failure of the specimen, but also reflect the axial stress–strain responses. We admit that the  $b$  value at point A is not very meaningful due that only very few AE

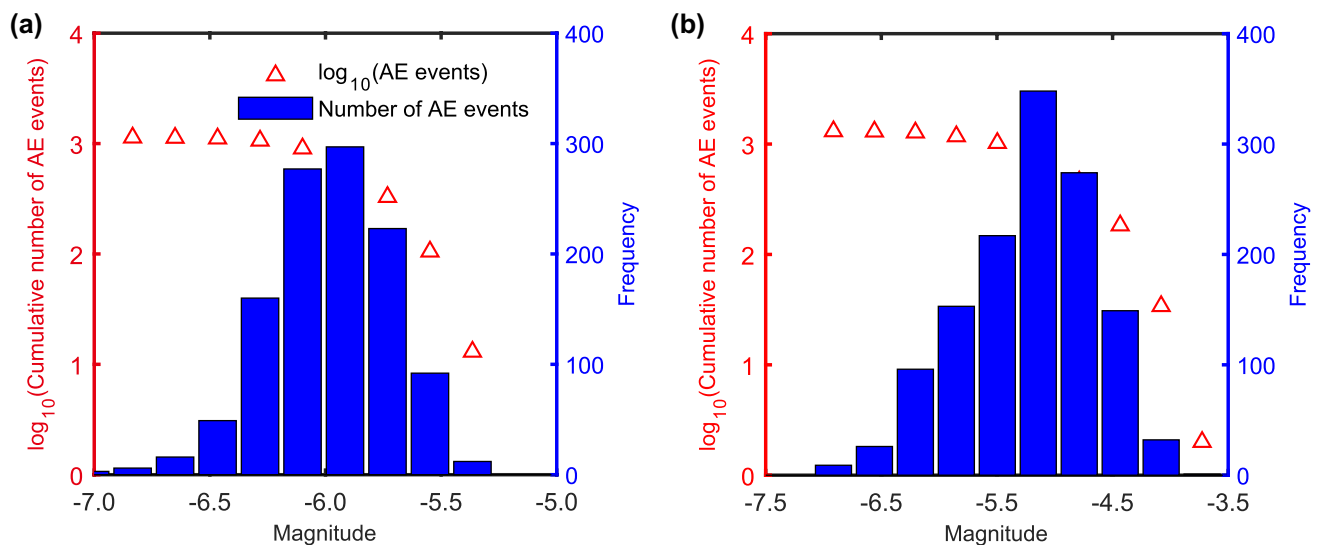


**Fig. 11** Frequency and the logarithm of cumulative AE event count as a function of AE magnitude for the AE events generated at loading point D in Fig. 9a. (a) Moment tensor-based AE simulation approach. (b) Energy based AE simulation approach (Lisjak et al. 2013)

events are generated at that moment; however, the  $b$  values around the peak point (e.g., from point B to D) are mainly distributed between 2.38 and 1.15, which are consistent with the experimental observations that generally ranging from 2.4 to 1.1 (Lockner 1993). Additionally, it is worth mentioning that if we treat each microcrack (i.e., the breakage of each cohesive element) as a separate and distinct AE event, i.e., without combining microcracks that are spatially and temporally connected as a distinct AE event, the  $b$  value at point D could be as large as 2.48, which is unreasonably larger than that in physical experiments. This manifests the necessity and appropriateness of our proposed clustering algorithm for more realistic AE simulations.

We further compare the moment tensor-based and energy-based AE simulation approach in terms of AE magnitude distribution for the events generated at loading point D in Fig. 9a and present the results in Fig. 11. It can be observed that the distribution range of AE magnitude for the energy-based AE simulation (Fig. 11b) is wider than that of the moment tensor-based AE simulation (Fig. 11a). This may be caused by the inherent difference between the two methods for AE magnitude estimation (Gutenberg 1956; Hanks and Kanamori 1979). In FDEM, the strain energy stored in triangular elements can be converted into kinetic, fracture, and friction energy. The kinetic energy change is used to capture the characteristics of AE events when a new fracture is initiated. However, accurate estimation of strain energy release is difficult in FDEM due to the utilization of constant-strain triangular elements. Consequently, the distribution range of AE magnitude using the two methods is expected to differ. Fortunately, the AE magnitude obtained from the two methods all tends to display power law distributions, which

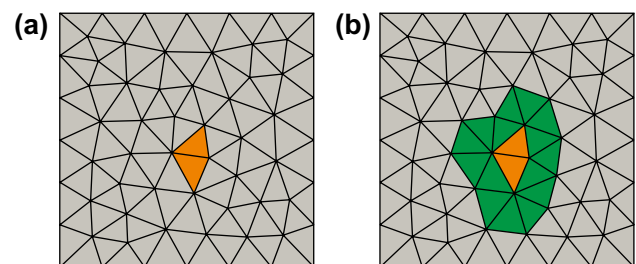


**Fig. 12** (a) Source area (original AE source area shown in Fig. 4). (b) Expanded AE source area

indicates the reasonableness of the two methods for capturing the distribution of AE magnitude. Notably, based on moment tensor decomposition, the proposed method not only inherits the advantage of capturing the spatial-temporal distribution of AE event magnitude, but also provides a valuable perspective to quantify and uncover the failure mechanism based on moment tensor decomposition.

To compare the influence of AE source area considered in AE magnitude calculation, we expand the region of an AE source area from the one denoted by the yellow patch shown in Fig. 12a to the yellow and green patch shown in Fig. 12b. Still based on the AE events generated at loading point D in the case shown in Fig. 9, their difference in AE magnitude distribution is analyzed. No doubt, the radius of the generated AE events is larger when the expanded source area is used, and the calculated magnitude of AE events is enlarged. However, as illustrated in Fig. 13, the distribution ranges of AE magnitude obtained using the original source area (Fig. 12a) and the expanded source area (Fig. 12b) are very

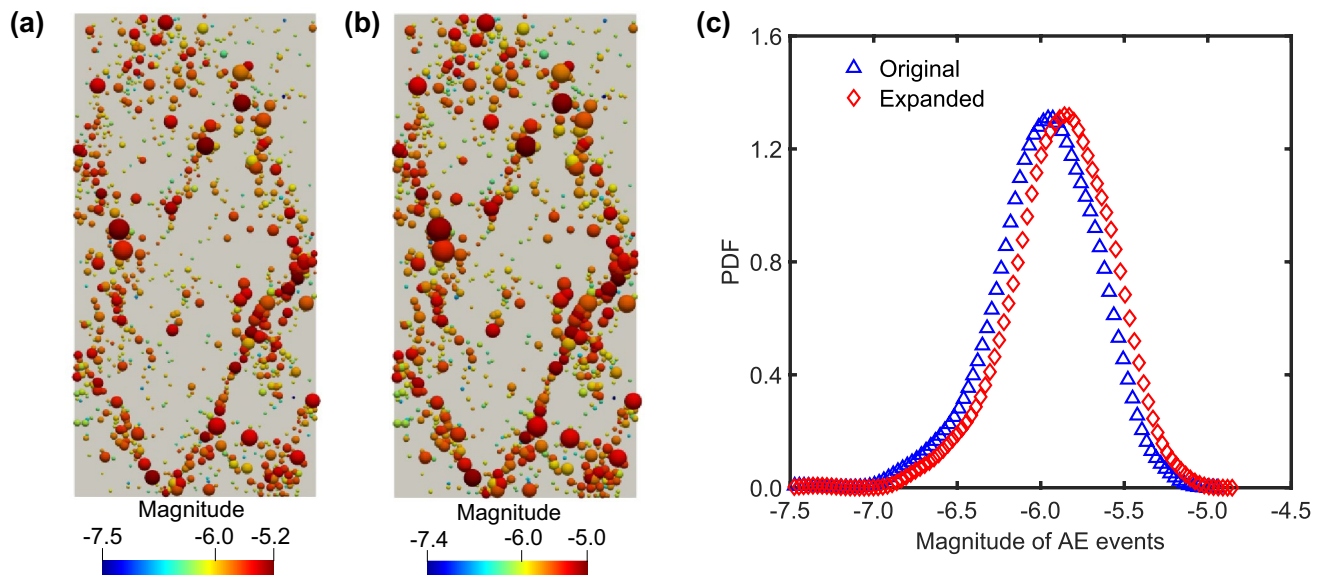


**Fig. 13** The distribution of AE magnitude for the events generated at loading point D in the case shown in Fig. 9 using different AE source areas: (a) source area defined in this manuscript, (b) expanded AE

source area. (c) PDFs (Probability Density Function) of AE events magnitude obtained using the two types of AE source areas

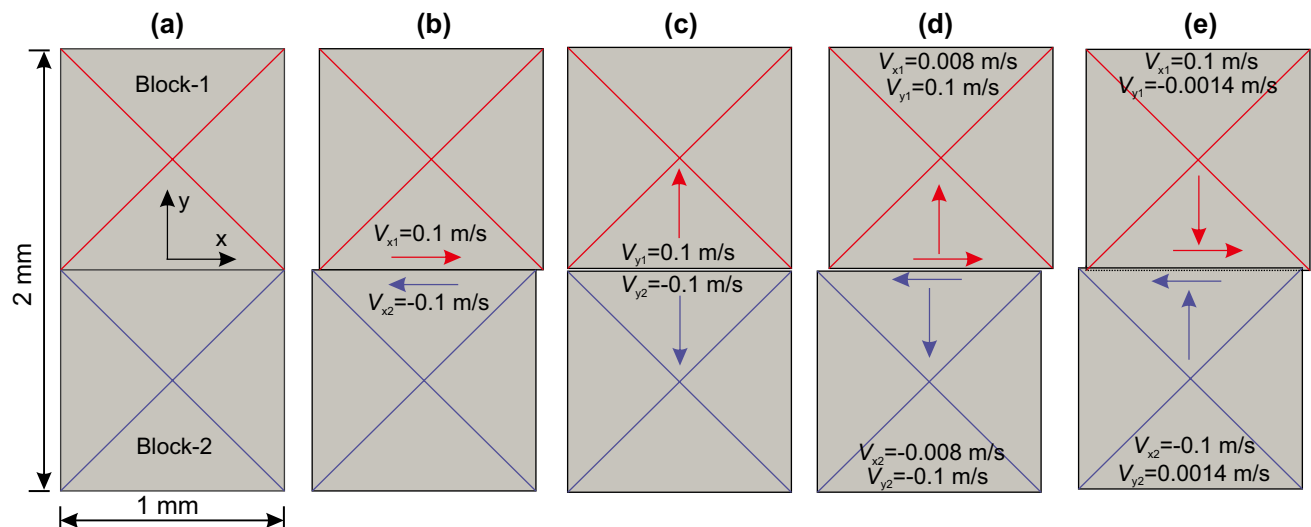


**Fig. 14** Models for testing Cra-DC and Cra-R. (a) Model dimensions and meshes. (b) Shear test. (c) Tensile test. (d) Tensile-shear test. (e) Compressive-shear test. The model consists of two blocks, denoted

as Block-1 and Block-2, respectively.  $V_{x1}$ ,  $V_{y1}$ , and  $V_{x2}$ ,  $V_{y2}$  are the velocities of Block-1 and Block-2, respectively, where the subscripts 'x' and 'y' denote the coordinate axis

close, which are  $-7.5$  to  $-5.2$  and  $-7.4$  to  $-5.0$ , respectively. The PDF (Probability Density Function) of AE magnitude using the expanded AE source area is located slightly to the right compared to the results using the original AE source area. Because of this insignificant difference between the results using these two types of AE source areas, also considering the computation cost, we currently prefer using the original AE source area shown in Fig. 12 in the following discussion.

## 4.2 Validation for Microcrack Types

Since the microcrack (i.e., the breakage of a single cohesive element) type can be directly obtained in FDEM simulations, to further validate the effectiveness of our proposed moment tensor-based AE simulation technique, four typical tests, i.e., shear, tensile, tensile-shear and compressive-shear tests, based on a single cohesive element, are specially designed to check the applicability of the two approaches

(i.e., Cra-DC and Cra-R) introduced in Sect. 3.3 for distinguishing the full spectrum of AE source types. The dimensions of the testing model are 1 mm × 2 mm (width × height) (Fig. 14a). Each model consists of two rock blocks (Block-1 and Block-2), and each block contains four triangular elements. We mainly focus on the cohesive element embedded between the two blocks. The physical–mechanical properties used for the four tests follow those in the previous literature (Euser et al. 2019). Here, the velocities imposed on Block-1 and Block-2 in each test are in opposite directions but with the same magnitude, and each generated AE event only contains a single microcrack. To induce pure shear and pure tensile cohesive element breakages, a velocity of 0.1 m/s is applied on both blocks along the  $x$  and  $y$  axis, respectively (Fig. 14b, c, respectively). For tensile-shear mixed breakage, velocities of 0.008 m/s and 0.1 m/s are applied along  $x$  and  $y$  axis, respectively (Fig. 14d). For compressive-shear mixed breakage, velocities of 0.1 m/s and 0.0014 m/s are applied along  $x$  and  $y$  axis, respectively (Fig. 14e). The magnitudes and directions of the imposed velocities on the two blocks are indicated in Fig. 14b–e. Note that the loading velocities for the four tests, especially the combinations of the  $x$  and  $y$  velocities in Fig. 14d, e, are carefully selected after a series of trial and error, which not only ensure the stability of computation, but also guarantee that the models can generate the prescribed AE event types.

The calculated  $C_{DC}$  and  $R$  values based on the obtained AE moment tensor for the four tests are tabulated in Table 2. In the pure shear test (Fig. 14b), the calculated  $C_{DC}$  and

$R$  factors are 100% and 0, respectively, validating the pure shear-type microcrack (see Fig. 7). In the pure tensile test (Fig. 14c), the  $C_{DC}$  and  $R$  are 0 and 50, respectively, again, verifying that the microcrack is of pure tensile type (see Fig. 7). Therefore, both methods can adequately determine pure shear and pure tensile type AE events. For the tensile-shear test (Fig. 14d), the  $C_{DC}$  is 54.2%, which is indeed located within the range of tensile-shear mixed type ( $40\% \leq C_{DC} \leq 60\%$ ); while  $R = 21.93$  only indicates a shear-type microcrack ( $-30 \leq R \leq 30$ ). However, since this  $R$  value is very close to the boundary between shear and tensile type (i.e.,  $R = 30$ ), we would instead deem this microcrack to have a transitional type between shear and tensile, i.e., a tensile-shear mixed type. Upon this, although the tensile-shear mixed type is not explicitly defined in the original Cra-R criterion, we may find an  $R$  value ranging around  $R = 30$  for the tensile-shear mixed AE type. In the compressive-shear test (Fig. 14e), the  $C_{DC}$  is 8.33%, which erroneously signifies a tensile type microcrack; this also tells that a re-definition of compressive-shear AE type in Cra-DC seems impossible. However,  $R = -45.83$  correctly captures the compressive-shear mixed type. Therefore, this last test demonstrates that the Cra-DC fails to identify compressive-shear mixed AE event, which verifies our suspicion mentioned earlier in Sect. 3.3.

We then change the loading velocities of the two blocks in the last two test scenarios shown in Fig. 14d and e to further systematically examine the capability of Cra-DC and Cra-R for distinguishing mixed AE types such as tensile-shear and compressive-shear, respectively. For the model under tensile-shear loading condition (Fig. 14d), we create a series of tests by varying the horizontal velocity in each test from 0.002 m/s to 0.020 m/s with an increment of 0.002 m/s, while the vertical velocity is fixed at 0.01 m/s, which are supposed to generate a transition of AE source type from tensile to tensile-shear mixed and then to shear. As can be

**Table 2** Results of the Cra-DC and Cra-R for the four testing models

Methods	Shear	Tensile	Tensile-shear	Compressive-shear
Cra-DC (% $C_{DC}$ )	100	0	54.2	8.33
Cra-R ( $R$ )	0	50	21.93	-45.83

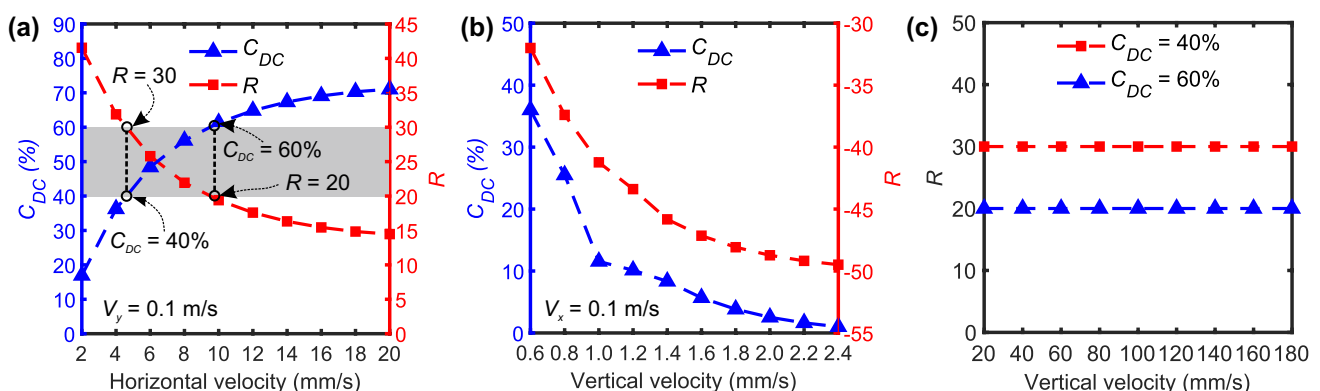


**Fig. 15** Comparison of Cra-DC and Cra-R with various horizontal and vertical velocities. (a) Tensile-shear test with horizontal velocity varying from 0.002 m/s to 0.020 m/s. (b) Compressive-shear test with

vertical velocity varying from 0.0006 m/s to 0.0024 m/s. (c) Corresponding  $R$  values with different vertical velocities when  $C_{DC}$  reaches 40% and 60% via tensile-shear tests

seen from the results presented in Fig. 15a, the resulting  $C_{DC}$  increases from 16.92 to 71.10% with the increasing horizontal velocity, which adequately captures the prescribed transition of AE source type; similarly, the  $R$  value decreases from 41.54 to 14.47, which apparently transits from tensile type to shear type. To find the appropriate  $R$  value range to define the tensile-shear mixed AE type in Cra-R, we first evaluate the two  $R$  values corresponding to the upper and lower boundaries of tensile-shear mixed AE type in Cra-DC (i.e.,  $C_{DC}=60\%$  and  $40\%$ ) based on the curves shown in Fig. 15a, which give  $R=20$  and  $30$  roughly, respectively. To further verify the boundaries for tensile-shear mixed AE type in Cra-R, we continue to perform a series of tensile-shear tests using the same model but vary the vertical velocity from 0.02 m/s to 0.18 m/s with an increment of 0.02 m/s and adjust the horizontal velocity accordingly through trial and error in order to find the appropriate combination of vertical and horizontal velocities that just generate a  $C_{DC}$  value of either 60% or 40%. The corresponding  $R$  values for these tests are presented in Fig. 15c, which are, respectively, 20 and 30. This confirms that the range of  $20 < R \leq 30$  in Cra-R could be preserved for tensile-shear mixed AE type, and we thus reach an improved version of the previous Cra-R criterion so that it is capable of identifying the full-spectrum AE source types (Fig. 16).

For the model subjected to compressive-shear loading condition (Fig. 14e), we also conduct a series of tests by changing the vertical velocity from 0.0006 m/s to 0.0024 m/s with an increment of 0.0002 m/s and fixing the horizontal velocity at 0.01 mm/s. Again, selecting these velocities can ensure the generation of distinct compressive-shear mixed AE events. Here, the vertical velocity is far smaller than the horizontal velocity since the compressive-shear failure is very sensitive to the vertical velocity. As can be seen from the results shown in Fig. 15b, with the increase of vertical velocity, the  $C_{DC}$  decreases from 36 to 1%, which inadequately indicates that the induced AE events are all of tensile type; the  $R$  decreases from  $-32$  to  $-49$ , which successfully validates that the mixed AE source is of

compressive-shear type. Again, Cra-DC fails to distinguish the compressive-shear AE sources, which is consistent with the previous theoretical explanations (Vavryčuk 2014) as well as our earlier suspicion mentioned in Sect. 3.3.

From the above analyses, we can conclude that, compared with Cra-DC, the Cra-R approach is more versatile for distinguishing the full spectrum AE source types. In the subsequent sections, we will adopt the improved Cra-R criterion illustrated in Fig. 16 to distinguish the macro-fracture types. As can be seen from Fig. 16, an AE event can be classified into four typical types, i.e., compressive-shear type if  $-100 \leq R \leq -30$ , shear type if  $-30 < R \leq 20$ , tensile-shear type if  $20 < R \leq 30$ , and tensile type if  $30 < R \leq 100$ .

### 4.3 Distinguishment of Macro-fracture Types

On the basis of the above validation of the implemented moment tensor-based AE simulation approach in FDEM for AE type identification, we re-employ the uniaxial compression test conducted in Sect. 4.1 to demonstrate further the capability of the proposed approach for distinguishing macro-fracture types based on the improved Cra-R criterion. Here, nine representative AE events are taken from the test at the time when the axial stress dropped to 31.17 MPa (i.e., point D in Fig. 9a). As presented in Fig. 17a, the nine events are successively numbered as AE- $i$  ( $i=1, 2, \dots, 9$ ) according to their first occurrence time, and each AE event contains multiple microcracks. The magnitudes of the selected AE events are mainly within the range of  $-5.6$  to  $-5.2$ , and the macro-fracture corresponding to each event contains microcracks of different types (see the damage type values of each microcrack calculated using Eq. (10) and shown in Fig. 17b).

The number of tensile, mixed and shear microcracks contained in the nine AE events are listed in Table 3, together with the  $R$  values calculated based on the corresponding AE moment tensors. According to the improved Cra-R criterion, we can see that for AE-1, AE-3, AE-7 and AE-8, their macro-fracture type is consistent with the dominant microcrack type. However, for AE-4 and AE-9, although tensile

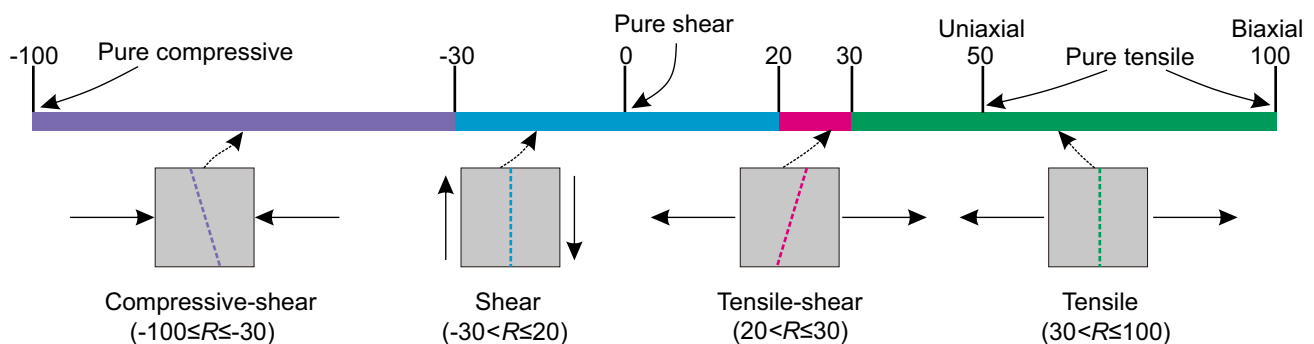
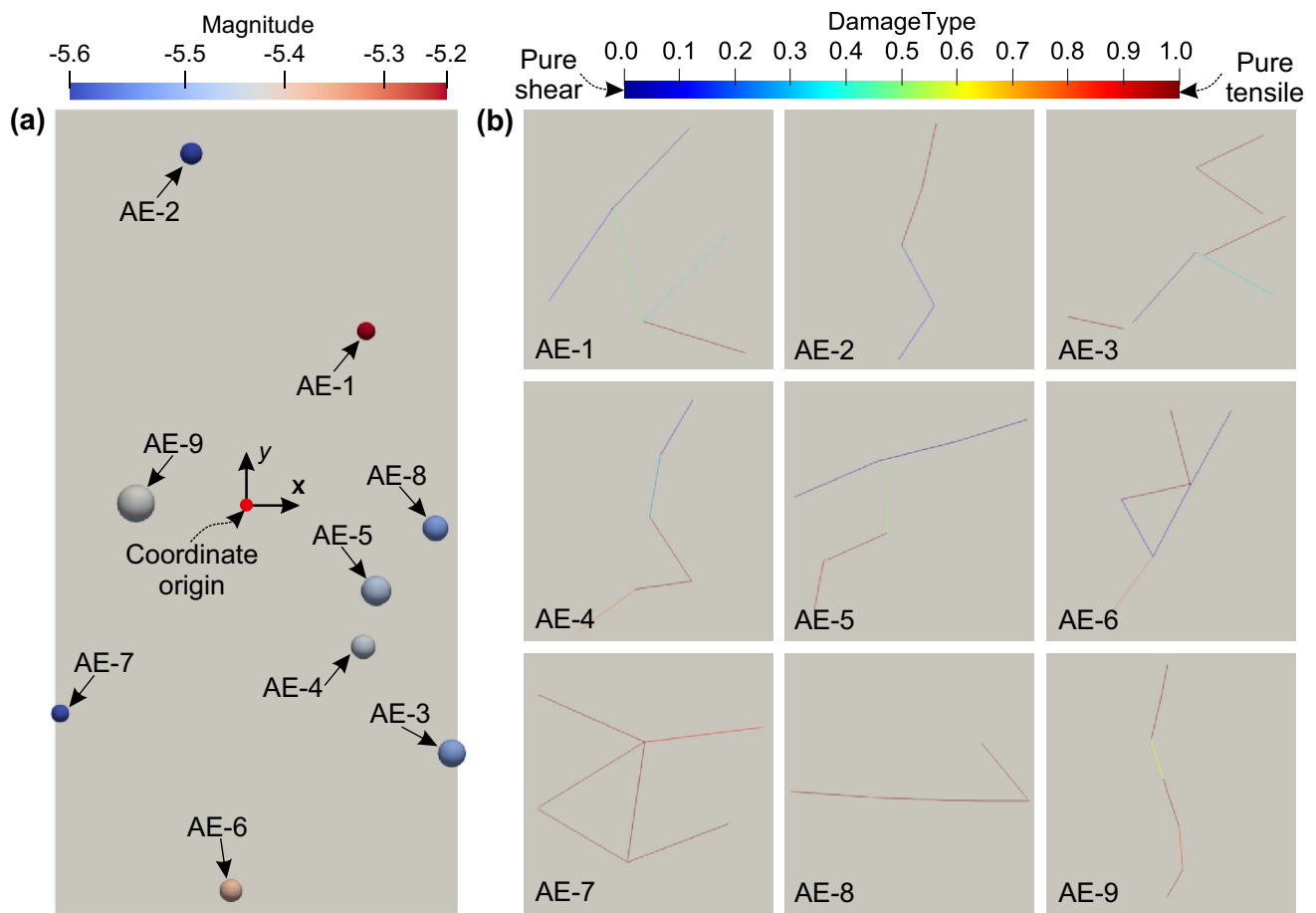


Fig. 16 The scale of improved Cra-R criterion for full spectrum AE source type distinguishment



**Fig. 17** Demonstration of the nine selected typical AE events and the corresponding macro-fractures. (a) Location of the nine AE events in the rock model. (b) The involved microcracks for each AE event. The coordinate origin is marked by a red dot in Fig. 17a

**Table 3** The number of tensile, mixed and shear microcracks contained in the nine selected AE events

AE events	Coordinates (mm)*	Number of microcracks			R	Macro-fracture type
		Tensile	Mixed	Shear		
AE-1	(14.7, 24.2)	1	3	1	-49.28	Compressive-shear
AE-2	(-8.7, 48.1)	2	0	2	-27.11	Shear
AE-3	(26.2, -32.5)	4	1	1	58.70	Tensile
AE-4	(14.3, -18.2)	3	1	1	8.89	Shear
AE-5	(16.2, -10.7)	1	2	3	49.52	Tensile
AE-6	(-34.2, -51.0)	2	2	2	46.01	Tensile
AE-7	(-26.3, -27.2)	4	1	1	48.65	Tensile
AE-8	(-24.0, -2.3)	4	0	0	56.66	Tensile
AE-9	(-16.2, 1.1)	4	2	0	-8.82	Shear

\*The coordinate origin coincides with the center of the specimen marked by a red dot in Fig. 17a

microcracks are dominant, their macro-fractures are of shear type. The opposite occurs for AE-5. Equal number of tensile, mixed and shear microcracks are found in AE-6, while the corresponding macro-fracture is of tensile type. A similar phenomenon can be seen in AE-2. These demonstrate that we cannot straightforwardly determine the macro-fracture

type simply based on the dominant type of microcracks contained in an AE event.

This is not uncommon in practice. Although many efforts have been made to investigate the mechanism of tensile and shear fractures from laboratory tests to field observations, it is still challenging to determine if a macroscopic shear

fracture involves only a shear mechanism or a combination of tensile and shear (Einstein 2021). Tensile fractures have similar problems. Wong and Einstein (2009) observed that the initiation region of a shear band consists of multiple vertically oriented tensile microcracks, which are almost parallel to the vertical loading direction. Furthermore, shear localization in granites results from the evolution of local tensile cracks (Doz and Riera 2000). This indicates that the shear-type macro-fracture may consist of both tensile and shear microcracks, and thus demonstrates that our newly implemented AE simulation approach in FDEM based on moment tensor provides an effective technique to explore the source type of macro-fractures. In the next section, by analyzing the evolution of macro-fractures in a bridge region between two pre-existing flaws in a rock specimen, we further demonstrate the advantage of the moment tensor-based AE simulation approach in rock mechanics.

#### 4.4 Failure Mechanism in Rock Bridge Region

To apply the moment tensor-based AE simulation approach, we establish a numerical model in FDEM to analyze the failure mechanism in a rock bridge region of two pre-existing flaws through laboratory-scale uniaxial compression tests similar to that in Wong and Einstein (2009). We first conduct a series of regular uniaxial compression and Brazilian tension tests in FDEM to explore the appropriate input mechanical parameters that guarantee the consistency of material behavior in our simulations with the existing laboratory tests (Wong and Einstein 2009). Both types of tests use the same models presented in Fig. 18: for the uniaxial compression tests, the model geometry  $H$  and  $W$  are,

respectively, 152 mm and 76 mm; for the Brazilian tension tests, the model diameter is  $D=76$  mm. Axial compression loads are imposed on the top and bottom of each specimen through two rigid platens moving in opposite directions at a constant velocity of 0.05 m/s. The nominal element size is set as 1.2 mm, and the unstructured Delaunay triangulation mesh scheme is utilized (see Fig. 18). Note that the simulation material is considered to be homogeneous, isotropic, and under plane stress conditions to avoid additional influencing factors on AE generation. As shown in Fig. 19, the compressive strength ( $\sigma_c$ ) and tensile strength ( $\sigma_t$ ) for the two models are 33.65 MPa and 3.26 MPa respectively, which matches the reported experimental value of 33.85 MPa and 3.2 MPa (Wong and Einstein 2009). This parameter calibration forms the basis for further investigation of the failure mechanism using the implemented AE simulation approach. The final reached model input parameters for the uniaxial compression tests with pre-existing flaws are tabulated in Table 4. More details on parameter calibration can be found in previous works (Deng et al. 2021; Liu and Deng 2019; Tatone and Grasselli 2015).

The model for the uniaxial compression tests with pre-existing flaws is presented in Fig. 20, which has dimensions of 76 mm  $\times$  152 mm (width  $\times$  height), and contains two 16 mm long pre-existing flaws with the same inclination angle  $\alpha=45^\circ$  (counted anticlockwise from the right). The distance between the center of the two pre-existing flaws is  $d=10$  mm, and the rock bridge region is marked by a green patch. Note that the loading velocity and element size are identical to the two tests mentioned above. Again, we select four loading points on the stress–strain curve, i.e., points A, B, C, and D shown in Fig. 21a, corresponding to the axial

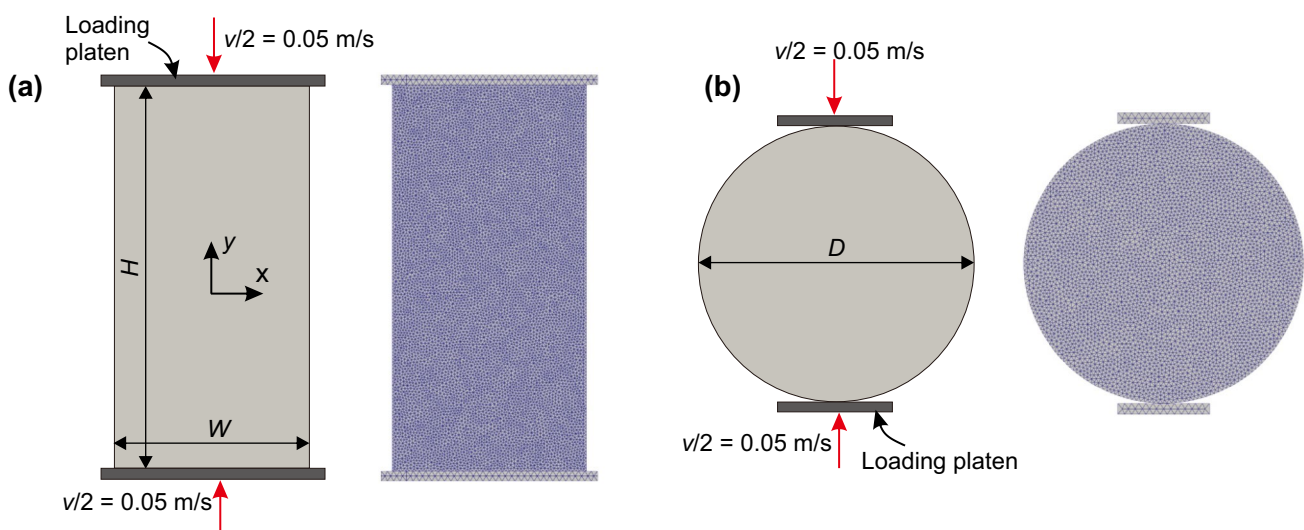


**Fig. 18** Geometrical and numerical models for tests of (a) uniaxial compression (b) Brazilian tension. The model geometry  $H$  and  $W$  for uniaxial compression test are, respectively, 152 mm and 76 mm; the model diameter for the Brazilian tension tests is  $D=76$  mm

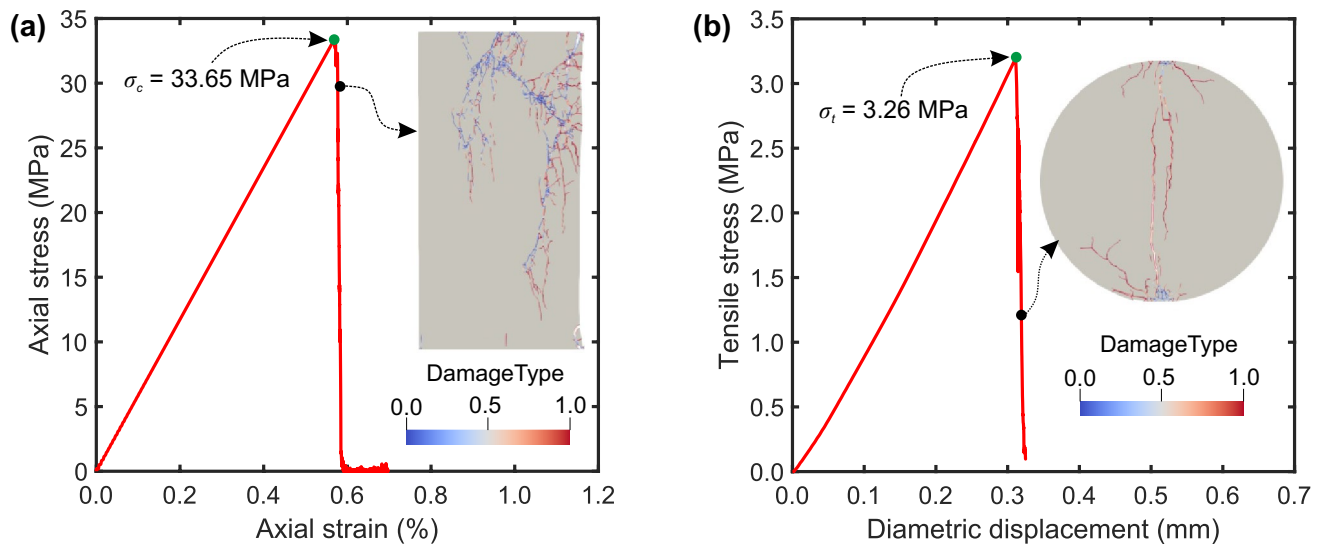


**Fig. 19** Results of the (a) uniaxial compression and (b) Brazilian tension tests for parameter calibration. The compressive and tensile strength are presented by  $\sigma_c$  and  $\sigma_t$ , respectively

**Table 4** Input parameters in FDEM simulations for uniaxial compression tests with pre-existing flaws

Input parameters	Values
Young's modulus, $E$ (GPa)	5.96
Bulk density, $\rho$ (kg/m <sup>3</sup> )	1540
Poisson's ratio, $\nu$	0.15
Viscous damping coefficient, $\eta$ (kg/m·s)	3400
Tensile strength, $f_t$ (MPa)	3.2
Cohesion, $c$ (MPa)	15.2
Internal friction angle, $\varphi$ (°)	30
Mode I fracture energy, $G_{f1}$ (J/m <sup>2</sup> )	5
Mode II fracture energy, $G_{f2}$ (J/m <sup>2</sup> )	20
Normal contact penalty, $P_n$ (GPa)	596
Tangential contact penalty, $P_s$ (GPa)	596
Cohesive penalty, $P_f$ (GPa)	596
Sample-plate friction coefficient, $k_1$ (—)	0.1
Sample friction coefficient, $k_2$ (—)	0.7

stress of 3.55 MPa, 10.26 MPa, 12.69 MPa and 8.3 MPa, respectively, to investigate the evolution of macro-fracture types.

The results presented in Fig. 21b demonstrate that wing cracks are initiated from the tips of pre-existing flaws when the axial stress reaches point A. Only three AE events are generated in the rock bridge region. According to the improved Cra-R criterion, the corresponding AE event types (i.e., macro-fracture type) are mainly tensile and tensile-shear (Fig. 22a). This is consistent with the dominant microcrack type indicated by the damage value distributions (Fig. 22a), demonstrating that wing cracks are essentially

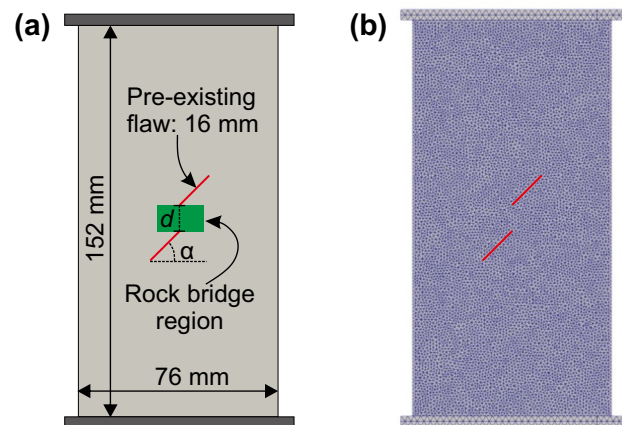


**Fig. 20** The uniaxial compression test model with two pre-existing parallel flaws. (a) Model geometry. (b) Mesh. The  $\alpha$  is the inclination angle of the pre-existing flaws (counted anticlockwise from the right). The distance between the tips of two pre-existing flaws is  $d=10$  mm, and the rock bridge region is marked by a green patch

tensile from both macro and micro perspectives. When the axial stress increases to point B, the stress–strain curve exhibits fluctuations, and wing cracks continue propagating along the maximum principal stress (Fig. 21c). Meanwhile, the crack coalescence accompanied by macroscopic shear and tensile types is observed in the rock bridge region (Fig. 22b). When the axial stress reaches the peak at point C (Fig. 21d), some microcracks continue to be generated in the rock bridge region, while only two new AE events are generated (Fig. 22c). Interestingly, the macro-fracture of compressive-shear first occurs in the rock bridge region, and the number of compressive-shear and shear macro-fractures

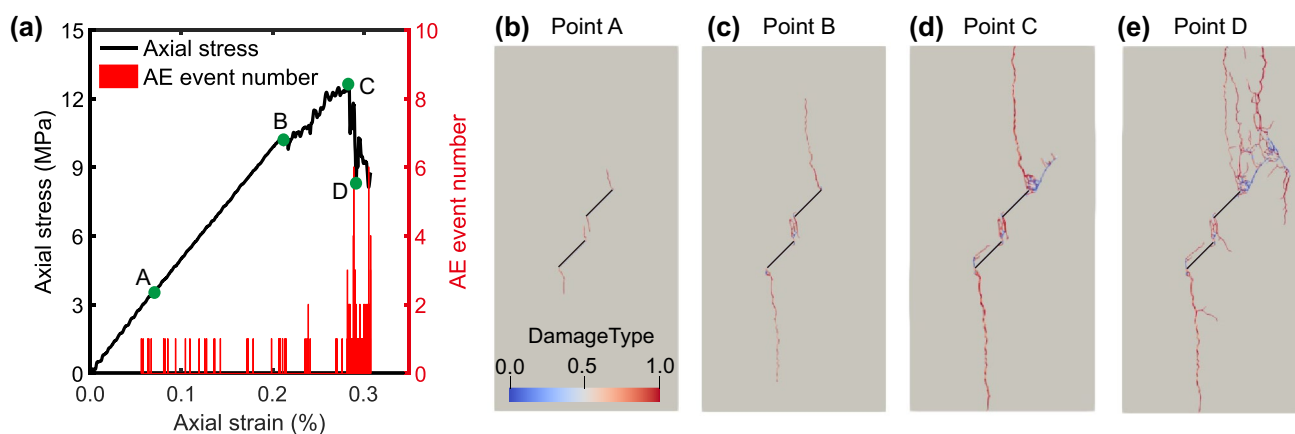


**Fig. 21** Axial stress and AE event number versus axial strain. Crack propagation and coalescence at the four loading points on the stress–strain curve shown in **a**: **(b)** point A, **(c)** point B, **(d)** point C and **(e)**

point D. The corresponding axial stresses at points A, B, C, and D are, respectively, 3.55 MPa, 10.26 MPa, 12.69 MPa and 8.3 MPa

is around half of the total number of AE events, although the tensile microcracks dominate. As the axial stress drops to point D (Fig. 21e), tensile microcracks also contribute to the significant increase of total microcracks, while the number of compressive-shear fracturing continues to increase (Fig. 22d).

Before the peak stress point C, the number of AE number increases stably, and the initiation and propagation of wing cracks (i.e., tensile cracks) dominate the fracturing around the rock bridge region. For the fracture process from Point C to D, the failure mechanism in the rock bridge region becomes more complex, which consists of four macro-fracture types. Notably, the macro-fractures of shear or compressive-shear increase, although the number of tensile microcracks still dominates (~70–75%). Consequently, the shear band region around the rock bridge may be induced by the tensile microcracks when crack coalescence occurs after the peak stress.

## 5 Conclusions

In this study, we have implemented a moment tensor-based AE simulation approach in FDEM considering the clustering of microcracks occurred close in space and time to investigate the rock fracturing procedure and the associated seismic behavior. The technique can not only accurately capture the distribution of AE event magnitude, but also effectively distinguish the type of the corresponding fractures and quantify the rock failure mechanism.

The capability of the AE simulation approach in capturing the distribution of AE event magnitude is firstly verified by establishing a heterogeneous rock model under uniaxial compressive load. We observe that the distribution of AE magnitude and the variation of  $b$  value are consistent with the axial stress–strain responses, which are also similar to

previous laboratory experiments. Specifically, prior to the axial peak stress, the number of AE events and the  $b$  value witness a steady increase and decrease, respectively, which corresponds to the nonlinear behavior of the stress–strain curve; the AE events of lower magnitude are randomly distributed in the specimen, and only the initiation of scattered microcracks is occurred, which leads to a continuous accumulation of strain energy. After the peak stress, the number of AE events and the  $b$  value show a sharp increase and decrease, respectively, which is accompanied by the propagation and coalescence of microcracks and the formation of throughgoing macro-fractures. Therefore, a combined analysis of AE magnitude and stress–strain responses may enhance the understanding of the progressive fracturing process in rocks.

By performing four microscale tests based on the breakage of a single cohesive element, the effectiveness of the moment tensor-based approach for distinguishing the source mechanism of AE event is validated, and the advantages and disadvantages of the pre-existing methods in distinguishing fracture types are compared. Then, based on our results, we revise the Cra-R criterion to better accommodate the tensile-shear fracture type, and thus reach an improved version of Cra-R criterion so that it is capable of distinguishing the full spectrum of AE source types (i.e., compressive-shear, shear, tensile-shear and tensile types). In addition, we have selected nine typical AE events formed in the uniaxial compression test and analyzed the macro-fracture types using the revised Cra-R criterion. The approach can accurately capture the type of macro-fracture regardless of the complex types of microcracks it contains, which demonstrates the capability of the proposed moment tensor approach for distinguishing macro-fracture types. Notably, we have found that the macro-fracture type cannot be straightforwardly determined based on the dominant type of microcracks contained in an

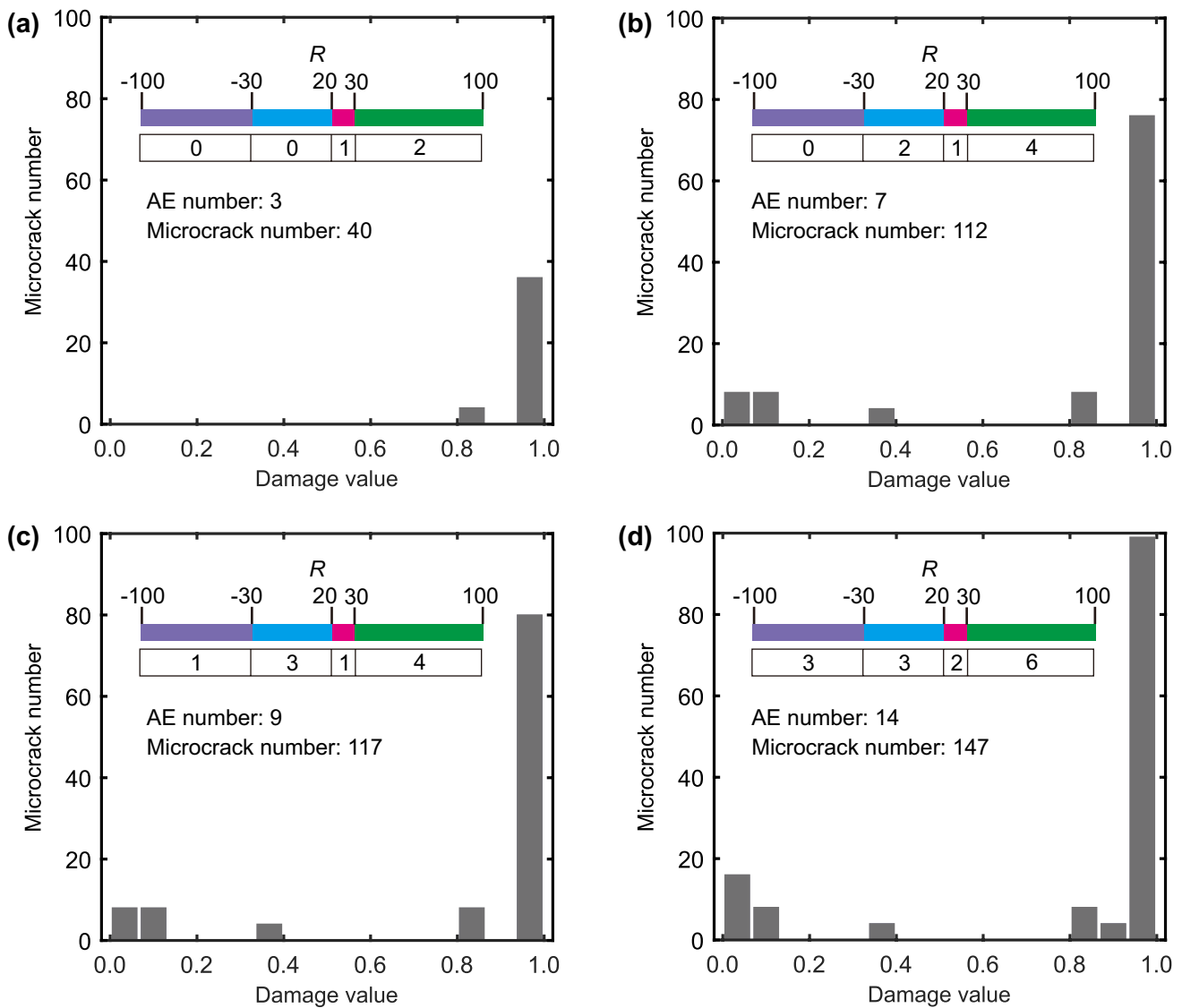


**Fig. 22** The type and the cumulative number of AE events and microcracks at the four loading points marked in Fig. 21a: (a) point A, (b) point B, (c) point C and (d) point D. Note that the damage value denotes the types of microcrack, i.e., 0 represents pure shear type,

1 represents pure tensile type, and others are of mixed type, which has been defined in Sect. 2.2. The *R* value indicates the types of AE events, which has been defined in Fig. 16

AE event. Through an exemplar application by analyzing the failure mechanism in a bridge region of two pre-existing flaws in a rock specimen, we demonstrate that the moment tensor-based AE simulation technique implemented in FDEM, together with our improved Cra-R criterion, may provide a new perspective to reveal the failure mechanism of fractures in rocks. The simulation results reveal that wing cracks are essentially tensile from both macro and micro perspectives, and the shear band region around the rock bridge may be induced by the tensile microcracks from a microscopic perspective. Additional work, including the implementation and comparison of different AE simulation

approaches, as well as their extensions to 3D models, will be reported in the near future.

**Acknowledgements** This work is supported by the Shenzhen Science and Technology Program (JCYJ20220530113612028), the Program for Guangdong Introducing Innovative and Entrepreneurial Teams (2017ZT07G264), the Shenzhen Science and Technology Innovation Committee (JCYJ20170817152743178), and the Shenzhen Peacock Plan (KQTD2017033114582189).

**Author contributions** The authors confirm contributions to the paper as below: research design: KG; analysis of numerical results: WC; draft manuscript preparation: WC; revised manuscript and funding support: KG, SW and WL. All authors have reviewed the results and approved the final version of the manuscript.

**Data Availability** The data are available by contacting the corresponding author upon reasonable request.

## Declarations

**Conflict of interest** The authors state that there are no known conflicts of interest associated with this publication.

## References

- Abdelaziz A, Zhao Q, Grasselli G (2018) Grain based modelling of rocks using the combined finite-discrete element method. *Comput Geotech* 103:73–81
- Aki K (1965) Maximum likelihood estimate of  $b$  in the formula  $\log N = a - bM$  and its confidence limits. *Bull Earthq Res Inst* 43:237–239
- Amitrano D, Grasso J-R, Hantz D (1999) From diffuse to localised damage through elastic interaction. *Geophys Res Lett* 26(14):2109–2112
- Backus GE (1977) Interpreting the seismic glut moments of total degree two or less. *Geophys J R Astron Soc* 51:1–25
- Cai M, Kaiser PK, Morioka H, Minami M, Maejima T, Tasaka Y, Kurose H (2007) FLAC/PFC coupled numerical simulation of AE in large-scale underground excavations. *Int J Rock Mech Min Sci* 44(4):550–564
- Castro-Filgueira U, Alejano LR, Ivars DM (2020) Particle flow code simulation of intact and fissured granitic rock samples. *J Rock Mech Geotech Eng* 12(5):960–974
- Chong Z, Li X, Hou P, Chen X, Wu Y (2017) Moment tensor analysis of transversely isotropic shale based on the discrete element method. *Int J Min Sci Technol* 27(3):507–515
- Cundall PA, Strack ODL (1979) A discrete numerical model for granular assemblies. *Geotechnique* 29(1):47–65
- Deng P, Liu Q, Huang X, Bo Y, Liu Q, Li W (2021) Sensitivity analysis of fracture energies for the combined finite-discrete element method (FDEM). *Eng Fract Mech* 251:107793
- Doz GN, Riera JD (2000) Towards the numerical simulation of seismic excitation. *Nucl Eng Des* 196(3):253–261
- Einstein HH (2021) Fractures: tension and shear. *Rock Mech Rock Eng* 54(7):3389–3408
- Euser B, Rougier E, Lei Z, Knight EE, Frash LP, Carey JW, Viswanathan H, Munjiza A (2019) Simulation of fracture coalescence in granite via the combined finite-discrete element method. *Rock Mech Rock Eng* 52(9):3213–3227
- Fang Z, Harrison JP (2002) Application of a local degradation model to the analysis of brittle fracture of laboratory scale rock specimens under triaxial conditions. *Int J Rock Mech Min Sci* 39(4):459–476
- Feignier B, Young RP (1992) Moment tensor inversion of induced microseismic events: evidence of non-shear failures in the  $-4 < M < -2$  moment magnitude range. *Geophys Res Lett* 19(14):1503–1506
- Feng X-T, Pan P-Z, Zhou H (2006) Simulation of the rock microfracturing process under uniaxial compression using an elasto-plastic cellular automaton. *Int J Rock Mech Min Sci* 43(7):1091–1108
- Ferguen N, Mebdoua-Lahmar Y, Lahmar H, Leclerc W, Guessasma M (2019) DEM model for simulation of crack propagation in plasma-sprayed alumina coatings. *Surf Coat Technol* 371:287–297
- Fukuda D, Mohammadnejad M, Liu H, Dehkhoda S, Chan A, Cho SH, Min GJ, Han H, Ji K, Fujii Y (2019a) Development of a GPGPU-parallelized hybrid finite-discrete element method for modeling rock fracture. *Int J Numer Anal Methods Geomech* 43(10):1797–1824
- Fukuda D, Mohammadnejad M, Liu H, Zhang Q, Zhao J, Dehkhoda S, Chan A, Kodama J-i, Fujii Y (2019b) Development of a 3D hybrid finite-discrete element simulator based on GPGPU-parallelized computation for modelling rock fracturing under quasi-static and dynamic loading conditions. *Rock Mech Rock Eng* 53(3):1079–1112
- Guo TY, Wong LNY (2021) Cracking mechanisms of a medium-grained granite under mixed-mode I–II loading illuminated by acoustic emission. *Int J Rock Mech Min Sci* 145:104852
- Gutenberg B (1956) The energy of earthquakes. *Q J Geol Soc* 112(1–4):1–14
- Gutenberg B, Richter CF (1942) Earthquake magnitude, intensity, energy, and acceleration. *Bull Seismol Soc Amer* 32(3):163–191
- Han H, Fukuda D, Liu H, Fathi Salmi E, Sellers E, Liu T, Chan A (2020a) FDEM simulation of rock damage evolution induced by contour blasting in the bench of tunnel at deep depth. *Tunn Undergr Space Technol* 103:103495
- Han H, Fukuda D, Liu H, Salmi EF, Sellers E, Liu T, Chan A (2020b) Combined finite-discrete element modelling of rock fracture and fragmentation induced by contour blasting during tunneling with high horizontal in-situ stress. *Int J Rock Mech Min Sci* 127:104214
- Hanks TC (1992) Small earthquakes. *Tectonic Forces Sci* 256(5062):1430–1432
- Hanks TC, Kanamori H (1979) A moment magnitude scale. *J Geophys Res* 84(B5):2348–2351
- Hazzard JF, Young RP (2000) Simulating acoustic emissions in bonded-particle models of rock. *Int J Rock Mech Min Sci* 37:867–872
- Hazzard JF, Young RP (2002) Moment tensors and micromechanical models. *Tectonophysics* 356:181–197
- He T-M, Zhao Q, Ha J, Xia K, Grasselli G (2018) Understanding progressive rock failure and associated seismicity using ultrasonic tomography and numerical simulation. *Tunn Undergr Space Technol* 81:26–34
- Jiang S, He M, Li X, Tang C, Liu J, Liu S (2020) Modeling and estimation of hole-type flaws on cracking mechanism of SiC ceramics under uniaxial compression: a 2D DEM simulation. *Theor Appl Fract Mech* 105:102398
- Jost ML, Herrmann RB (1989) A student's guide to and review of moment tensors. *Seismol Res Lett* 60(2):37–57
- Lei Q, Gao K (2018) Correlation between fracture network properties and stress variability in geological media. *Geophys Res Lett* 45(9):3994–4006
- Lei Q, Gholizadeh Doonechaly N, Tsang C-F (2021) Modelling fluid injection-induced fracture activation, damage growth, seismicity occurrence and connectivity change in naturally fractured rocks. *Int J Rock Mech Min Sci* 138:104598
- Lei X, Masuda K, Nishizawa O, Jouniaux L, Liu L, Ma W, Satoh T, Kusunose K (2004) Detailed analysis of acoustic emission activity during catastrophic fracture of faults in rock. *J Struct Geol* 26(2):247–258
- Li XF, Li HB, Liu LW, Liu YQ, Ju MH, Zhao J (2020) Investigating the crack initiation and propagation mechanism in brittle rocks using grain-based finite-discrete element method. *Int J Rock Mech Min Sci* 127:104219
- Lisjak A, Liu Q, Zhao Q, Mahabadi OK, Grasselli G (2013) Numerical simulation of acoustic emission in brittle rocks by two-dimensional finite-discrete element analysis. *Geophys J Int* 195(1):423–443
- Liu Q, Deng P (2019) A numerical investigation of element size and loading/unloading rate for intact rock in laboratory-scale and field-scale based on the combined finite-discrete element method. *Eng Fract Mech* 211:442–462
- Liu Q, Jiang Y, Wu Z, Qian Z, Xu X (2018) Numerical modeling of acoustic emission during rock failure process using a Voronoi element based – explicit numerical manifold method. *Tunn Undergr Space Technol* 79:175–189

- Lockner D (1993) The role of acoustic emission in the study of rock fracture. *Int J Rock Mech Min Sci* 30:883–889
- Mahabadi OK, Lisjak A, Munjiza A, Grasselli G (2012) Y-Geo: new combined finite-discrete element numerical code for geomechanical applications. *Int J Geomech* 12(6):676–688
- Martínez-Garzón P, Kwiatek G, Bohnhoff M, Dresen G (2017) Volumetric components in the earthquake source related to fluid injection and stress state. *Geophys Res Lett* 44(2):800–809
- Mohammadnejad M, Liu H, Chan A, Dehkoda S, Fukuda D (2018) An overview on advances in computational fracture mechanics of rock. *Geosystem Eng* 24(4):206–229
- Munjiza A (2004) The combined finite-discrete element method. John Wiley, London
- Munjiza A, Andrews KRF (1998) NBS contact detection algorithm for bodies of similar size. *Int J Numer Methods Eng* 43(1):131–149
- Munjiza A, Lei Z, Divic V, Peros B (2013) Fracture and fragmentation of thin shells using the combined finite-discrete element method. *Int J Numer Methods Eng* 95(6):478–498
- Munjiza AA, Knight EE, Rougier E (2011) Computational mechanics of discontinua. Wiley, London
- Ohtsu M (1995) Acoustic emission theory for moment tensor analysis. *Res Nondestruct Eval* 6(3):169–184
- Potyondy DO, Cundall PA (2004) A bonded-particle model for rock. *Int J Rock Mech Min Sci* 41(8):1329–1364
- Scholz CH (2019) The mechanics of earthquakes and faulting. Cambridge University Press
- Silver PG, Jordan TH (1982) Optimal estimation of scalar seismic moment. *Geophys J Int* 70(3):755–787
- Sun W, Wu S (2021) A study of crack initiation and source mechanism in the Brazilian test based on moment tensor. *Eng Fract Mech* 246:107622
- Tang C (1997) Numerical simulation of progressive rock failure and associated seismicity. *Int J Rock Mech Min Sci* 34:249–261
- Tang J-H, Chen X-D, Dai F (2020) Experimental study on the crack propagation and acoustic emission characteristics of notched rock beams under post-peak cyclic loading. *Eng Fract Mech* 226:106890
- Tatone BSA, Grasselli G (2015) A calibration procedure for two-dimensional laboratory-scale hybrid finite-discrete element simulations. *Int J Rock Mech Min Sci* 75:56–72
- Vavryčuk V (2014) Moment tensor decompositions revisited. *J Seismol* 19(1):231–252
- Wang B, Li H, Shao Z, Chen S, Li X (2021a) Investigating the mechanism of rock fracturing induced by high-pressure gas blasting with a hybrid continuum-discontinuum method. *Comput Geotech* 140:104445
- Wang Y, Deng H, Deng Y, Chen K, He J (2021b) Study on crack dynamic evolution and damage-fracture mechanism of rock with pre-existing cracks based on acoustic emission location. *J Pet Sci Eng* 201:108420
- Woessner J, Wiemer S (2005) Assessing the quality of earthquake catalogues: estimating the magnitude of completeness and its uncertainty. *Bull Seismol Soc Am* 95(2):684–698
- Wong LNY, Einstein HH (2009) Crack coalescence in molded gypsum and carrara marble: part 2—microscopic observations and interpretation. *Rock Mech Rock Eng* 42(3):513–545
- Xie HP, Liu JF, Ju Y, Li J, Xie LZ (2011) Fractal property of spatial distribution of acoustic emissions during the failure process of bedded rock salt. *Int J Rock Mech Min Sci* 48(8):1344–1351
- Xu W, Cao P (2018) Fracture behaviour of cemented tailing backfill with pre-existing crack and thermal treatment under three-point bending loading: experimental studies and particle flow code simulation. *Eng Fract Mech* 195:129–141
- Yan C, Wang T, Ke W, Wang G (2021) A 2D FDEM-based moisture diffusion–fracture coupling model for simulating soil desiccation cracking. *Acta Geotech* 2:2
- Yan C, Xie X, Ren Y, Ke W, Wang G (2022) A FDEM-based 2D coupled thermal-hydro-mechanical model for multiphysical simulation of rock fracturing. *Int J Rock Mech Min Sci* 149:104964
- Zhang Q, Zhang X-P (2019) The crack nature analysis of primary and secondary cracks: a numerical study based on moment tensors. *Eng Fract Mech* 210:70–83
- Zhang Q, Zhang X-P, Ji P-Q, Zhang H, Tang X, Wu Z (2020) Study of interaction mechanisms between multiple parallel weak planes and hydraulic fracture using the bonded-particle model based on moment tensors. *J Nat Gas Sci Eng* 76:103176
- Zhang X-P, Zhang Q (2017) Distinction of crack nature in brittle rock-like materials: a numerical study based on moment tensors. *Rock Mech Rock Eng* 50(10):2837–2845
- Zhao Q (2017) Investigating brittle rock failure and associated seismicity using laboratory experiments and numerical simulations. University of Toronto (Canada)
- Zhao Q, Lisjak A, Mahabadi O, Liu Q, Grasselli G (2014) Numerical simulation of hydraulic fracturing and associated microseismicity using finite-discrete element method. *J Rock Mech Geotech Eng* 6(6):574–581
- Zhao Q, Tisato N, Abdelaziz A, Ha J, Grasselli G (2023) Numerical investigation of progressive damage and associated seismicity on a laboratory fault. *arXiv preprint arXiv: 04033*
- Zhao Q, Tisato N, Grasselli G, Mahabadi OK, Lisjak A, Liu Q (2015) Influence of in situ stress variations on acoustic emissions: a numerical study. *Geophys J Int* 203(2):1246–1252
- Zhao Y, Zhao G, Zhou J, Ma J, Cai X (2021) Failure mechanism analysis of rock in particle discrete element method simulation based on moment tensors. *Comput Geotech* 136:104215

**Publisher's Note** Springer Nature remains neutral with regard to jurisdictional claims in published maps and institutional affiliations.

Springer Nature or its licensor (e.g. a society or other partner) holds exclusive rights to this article under a publishing agreement with the author(s) or other rightsholder(s); author self-archiving of the accepted manuscript version of this article is solely governed by the terms of such publishing agreement and applicable law.